Western Arctic Shelfbreak Eddies: Formation and Transport

MICHAEL A. SPALL, ROBERT S. PICKART, PAULA S. FRATANTONI, AND ALBERT J. PLUEDDEMANN

Woods Hole Oceanographic Institution, Woods Hole, Massachusetts

(Manuscript received 25 April 2007, in final form 27 November 2007)

ABSTRACT

The mean structure and time-dependent behavior of the shelfbreak jet along the southern Beaufort Sea, and its ability to transport properties into the basin interior via eddies are explored using high-resolution mooring data and an idealized numerical model. The analysis focuses on springtime, when weakly stratified winter-transformed Pacific water is being advected out of the Chukchi Sea. When winds are weak, the observed jet is bottom trapped with a low potential vorticity core and has maximum mean velocities of $O(25$ cm $s^{-1})$ and an eastward transport of 0.42 Sv (1 Sv $\equiv 10^6$ m^3 s^{-1}). Despite the absence of winds, the current is highly time dependent, with relative vorticity and twisting vorticity often important components of the Ertel potential vorticity. An idealized primitive equation model forced by dense, weakly stratified waters flowing off a shelf produces a mean middepth boundary current similar in structure to that observed at the mooring site. The model boundary current is also highly variable, and produces numerous strong, small anticyclonic eddies that transport the shelf water into the basin interior. Analysis of the energy conversion terms in both the mooring data and the numerical model indicates that the eddies are formed via baroclinic instability of the boundary current. The structure of the eddies in the basin interior compares well with observations from drifting ice platforms. The results suggest that eddies shed from the shelfbreak jet contribute significantly to the offshore flux of heat, salt, and other properties, and are likely important for the ventilation of the halocline in the western Arctic Ocean. Interaction with an anticyclonic basin-scale circulation, meant to represent the Beaufort gyre, enhances the offshore transport of shelf water and results in a loss of mass transport from the shelfbreak jet.

1. Introduction

The cold halocline of the interior western Arctic Ocean provides a barrier between the warmer, deeper waters of Atlantic origin and the sea surface, which is ice covered for most or all of the year. If these Atlantic waters were able to penetrate to the surface, there would be enough warm water to melt the ice cover. This would, of course, have enormous implications for the entire ecosystem of the Arctic, as well as for air–sea exchange and global climate. It is now generally accepted that the halocline waters originate from the shelf regions (Aagaard et al. 1981; Muench et al. 2000). However, fundamental aspects of this exchange are not well understood. For example, it is not clear where this exchange takes place, when during the year it occurs, or by what physical mechanisms it is accomplished.

One process that may play a role in halocline ventilation is eddy generation from the boundaries of the basin, where the most energetic circulation exists (Aagaard and Carmack 1994). The interior of the Canada Basin is populated with small eddies of $O(20$ km) diameter. Measurements from drifting ice platforms suggest that the eddies are overwhelmingly anticyclonic (>90%). Eddies appear to be concentrated in the halocline (50–150-m depth), although both deeper (Manley and Hunkins 1985; D'Asaro 1988a) and shallower (Pickart et al. 2005; Plueddemann and Krishfield 2008, manuscript submitted to *J. Geophys. Res.*, hereafter PLKR; Timmerman et al. 2008) eddies have been observed.[1] Eddies may be either warm or cold relative to the surrounding water, although cold-core eddies appear to dominate (Manley and Hunkins 1985). Measurements taken from drifting ice platforms suggest that one to two eddies are found every 100 km of drift (Hunkins 1974; Manley and Hunkins 1985; PLKR), and

Corresponding author address: Michael A. Spall, Woods Hole Oceanographic Institution, Woods Hole, MA 02543.
E-mail: mspall@whoi.edu

[1] It should be noted that near-surface eddies are difficult to detect from the historical ice camp data, so there may be a bias in these measurements.

DOI: 10.1175/2007JPO3829.1

it has been estimated that the basin is filled with 100–200 of these features at any one time (PLKR).

Hydrographic data suggest that the Canada Basin eddies are formed from distinct water masses, perhaps related to the winter and summer water masses on the Chukchi shelf (Pickart et al. 2005). The heat and salt transported seaward by the most commonly observed eddies are believed to be fundamental to the ventilation of the interior Arctic halocline (e.g., Muench et al. 2000). These eddies also represent a source of nutrients and zooplankton to the central basin (Llinas et al. 2008), and are potentially important for the off-shelf flux of organic carbon (Mathis et al. 2007). That far fewer of the eddies are found in the eastern Arctic suggests a source in the western basin (Manley and Hunkins 1985).

The idea that anticyclonic eddies observed in the interior Canada Basin originate from hydrodynamic instabilities of the Alaskan Coastal Current in summer was put forward by Hunkins (1974), Hart and Killworth (1976), and Manley and Hunkins (1985). Their results are suggestive only, however, because their linear stability analysis was limited to very idealized, one-dimensional flow with vertical shear typical of the boundary region. They did not consider a realistic structure of the boundary current (BC) or bottom topography, seasonality, or nonlinearities, all of which may influence the stability of the current and offshore eddy flux. Moreover, the eddies produced from this current would be surface intensified and contain warm water in their cores, and thus would be unable to explain the source of the subsurface, cold-core anticyclones observed so prevalently in the interior.

D'Asaro (1988b) proposed that anticyclonic vorticity generated by a frictional sublayer of the boundary current in Barrow Canyon might provide a means to produce the near-zero potential vorticity sometimes found in the anticyclones, and that eddies would be shed where the topography turns sharply to the right at the mouth of the canyon. Observations do not show such strong shear near the boundary (Münchow and Carmack 1997; Pickart et al. 2005), and it is more likely that the low potential vorticity of the eddies is due to the convective origin of their water masses in the Chukchi Sea.

A series of papers by Chao and Shaw (1996, 1998, 2002, 2003a,b) has explored the various means of generating anticyclonic Arctic eddies. Early papers showed that localized regions of buoyancy loss in the interior can give rise to patches of low potential vorticity water, which then adjust to form anticyclone–cyclone pairs (Chao and Shaw 1996, 1998). Stress applied to the upper-layer cyclone (representing ice interaction) leads to its decay, resulting in a middepth anticyclone. However, these experiments require forcing on very small scales (deformation radius) and of unrealistic strength in order to produce reasonably strong eddies. More recently, Chao and Shaw (2002, 2003a,b) have explored boundary current sources for the eddies. This series of papers provides a source of dense water on the shelf and adds various effects, such as a strong offshore baroclinic current (meant to represent the Beaufort gyre), a cross-shelf flux, a canyon, and an offshore undercurrent (meant to represent the Beaufort Undercurrent; Aagaard 1984). Under various circumstances, small numbers of cold-core, anticyclonic eddies are formed in these simulations [e.g., eddies associated with sinking dense water in Barrow Canyon; see Chao and Shaw (2003b)]. However, these authors have imposed an unrealistically strong westward-flowing Beaufort gyre along the boundary, instead of the eastward-flowing shelfbreak jet, which is now known to exist.

Historical measurements have revealed that Pacific-origin waters flow along the southern edge of the Canada Basin (e.g., Mountain et al. 1976; Aagaard 1984). Recent observations, including those from the western Arctic shelf–basin interactions (SBI) program, have elucidated this circulation. For example, it is now known that, in the absence of strong winds, an eastward-flowing boundary current exists along the edge of both the Chukchi and Beaufort Seas (Nikolopoulos et al. 2008, hereafter NIK; Mathis et al. 2007; Llinas et al. 2008; see also Fig. 1). It is a narrow jet (order 10–15 km), trapped in the shelf break, with different seasonal configurations. It is largely composed of water that entered the Arctic through the Bering Strait and subsequently reached the shelf edge via Herald Canyon in the west, and Barrow Canyon in the east (Fig. 1). More is known about the Beaufort shelfbreak jet because of a high-resolution mooring array that was maintained across the current during SBI (see NIK). There are three overall seasonal states of the current. During summer it is predominantly surface intensified and advects Alaskan coastal water; that is, it is the eastward extension of the Alaskan Coastal Current (see also Paquette and Bourke 1974; Mountain et al. 1976). During fall and winter the current becomes bottom trapped, but it often reverses (flows westward) under strong easterly winds (NIK; Llinas et al. 2008). Then, in spring, as the winds weaken, the current advects the cold, dense winter water formed the previous winter in the Chukchi and Bering Seas (Muench et al. 1988; Weingartner et al. 1998). In this configuration the current is bottom trapped, with the strongest eastward flow in the vicinity of the shelf break.

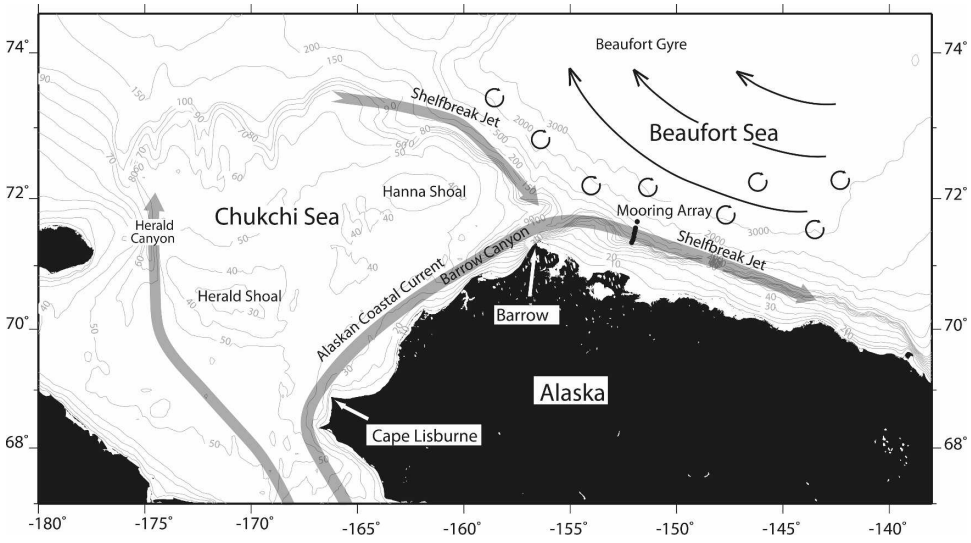

FIG. 1. Map of the region of interest and schematic circulation. A shelfbreak jet exists along the edge of the Chukchi and Beaufort Seas. In the Beaufort Sea it is fed by the Alaskan Coastal Current flowing through the Barrow Canyon, and in the Chukchi Sea it is presumably fed by the outflow from Herald Canyon. Anticyclonic eddies are commonly observed offshore of the shelfbreak jet and in the Canada Basin within the Beaufort gyre. The mooring locations of the SBI array are indicated.

In each of the above configurations the current is characterized by strong mesoscale variability. Some of this is wind driven [especially in fall and winter resulting from frequent storms; see Pickart and Moore (2008, manuscript submitted to *J. Geophys. Res.*, hereafter PM)], but some appears to stem from internal instabilities of the current. Using a collection of historical hydrographic sections, Pickart (2004) argued that the Beaufort shelfbreak jet should be baroclinically unstable. The observed pattern of temperature variance is maximum at the offshore edge of the boundary current at the depth of the upper halocline, consistent with baroclinic instability. Furthermore, synoptic sections from SBI have captured eddies being spawned from the current along the Chukchi shelf edge (Pickart et al. 2005; Mathis et al. 2007). These observations demonstrate that 1) eddies can be formed from the boundary current over the steep shelfbreak topography away from Herald and Barrow Canyons, 2) the spatial scales of the boundary current and eddies is $O(10\ \text{km})$, and 3) there is a seasonal cycle associated with the type of eddy that is formed from the boundary current.

In this study we use data from the SBI mooring array deployed across the Beaufort shelfbreak jet, observations of interior eddies from drifting platforms, and an idealized numerical model of the shelfbreak jet to investigate the mechanisms of eddy formation in the western Arctic. We focus on the spring time period, when the current is advecting the coldest Chukchi/Bering winter water, and we consider the "free jet" case when there is no wind forcing (in both the observations and the model). The characteristics and dynamics of this configuration of the boundary current are presented first using the SBI data. This is followed by the model investigation, which focuses on the dynamics of eddy formation and the associated flux of mass and properties into the interior. Aspects of the model boundary current, and the structure of the eddies that it forms, are compared with the mooring data and with the interior ice station data.

2. Free-jet configuration of the Beaufort shelfbreak current

a. Mooring data calibration and processing

From August 2002 to September 2004 a high-resolution mooring array was maintained across the Beaufort shelf break and slope as part of the SBI program. The array was situated near 152°W, approximately 150 km east of Barrow Canyon (Fig. 1). It consisted of conductivity–temperature–depth (CTD) profilers to measure the hydrography, and acoustic Doppler current profilers (ADCPs) and acoustic current meters to measure velocity. Moorings BS2–BS6 (Fig. 2) were spaced 3–5 km apart on the upper part of the slope that sampled the Pacific component of the boundary current. The offshore moorings (BS7–BS8) were generally outside of the boundary current (with near-zero or westward mean flow; see NIK). Because the CTD profilers on these two moorings sampled only

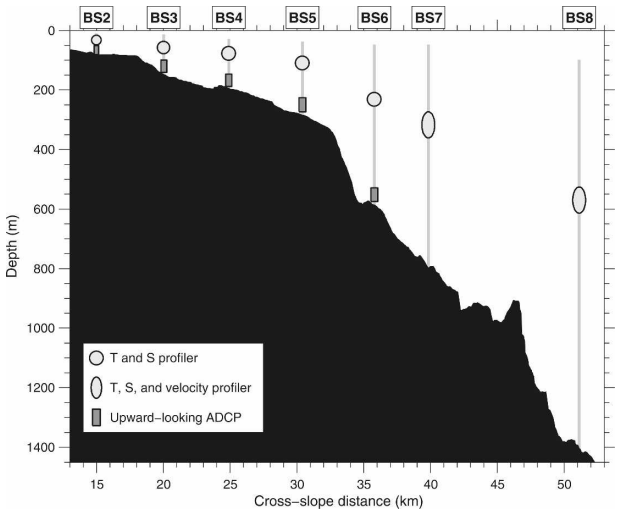

FIG. 2. Configuration of the SBI Beaufort slope-profiling mooring array.

half as frequently (because of battery constraints), the data from BS7–BS8 were not included in the present study. The onshore part of the array analyzed here provided four synoptic vertical sections per day of the hydrographic and velocity structure of the boundary current (each CTD section took approximately 45 min to occupy). The sections were objectively gridded using Laplacian spline interpolation onto a grid with 2-km spacing in the horizontal and 5-m spacing in the vertical. The velocity data were detided using the tidal constituents obtained from the raw hourly ADCP data,[2] and an along-stream direction was objectively defined using the first year of data (see NIK). The positive along-stream direction is 125°T, which is generally aligned with the topography upstream (west) of the array. The positive cross-stream direction is oriented offshore at 35°T.

The profiling CTD sensors were calibrated using stationary CTD sensors located at the bases of the moorings, together with shipboard CTD casts taken during the deployment and recovery cruises. The stationary sensors were themselves calibrated during the recovery cruises by attaching the sensors to the shipboard CTD package and performing comparison casts in deep water. The calibration and processing procedures are described in Fratantoni et al. (2006). The accuracy of the sensors was estimated to be 0.002°C for temperature and better than 0.03 for salinity. Because of potential ridging of the pack ice, the top floats of the moorings were positioned to be at 40 m. Although the velocity profiles extended shallower than this, the vertical sections were limited to the part of the domain where the hydrographic and velocity measurements overlapped; hence, the top 40 m are blank. This is not a problem for the present study because the boundary current is bottom intensified during the time period of interest.

Sections were constructed of potential temperature (θ), potential density (σ_θ, referenced to the sea surface), salinity (S), along-stream (u) and cross-stream (v) velocity, and the different components of the Ertel potential vorticity,

$$\pi = \frac{-f}{\rho_0}\frac{\partial \sigma_\theta}{\partial z} - \frac{1}{\rho_0}\left(\frac{\partial v}{\partial x} - \frac{\partial u}{\partial y}\right)\frac{\partial \sigma_\theta}{\partial z} - \frac{1}{\rho_0}\frac{\partial u}{\partial z}\frac{\partial \sigma_\theta}{\partial y}, \quad (1)$$

where f is the (constant) Coriolis parameter (1.45×10^{-4} s^{-1}), and ρ_0 is the reference density (1.028×10^3 kg m^{-3}, calculated using the mean array data). The first term on the right-hand side of (1) is the vertical stretching term, and the second term is the relative vorticity. Because we are working in a rotated coordinate system aligned with the general direction of the flow, the relative vorticity in the boundary current is dominated by the u_y term. The third term is the tilting vorticity [see Hall (1994) for a derivation of this term], which becomes important when the isopycnals slope strongly across the current (which happens in the Beaufort shelfbreak jet, see below).

b. Seasonal water masses

As mentioned in the introduction, there are three main seasonal configurations of the shelfbreak current. The velocity and hydrographic structure of each of these states is presented in NIK. The seasonal timing of the water masses can be seen in Fig. 3, which shows the temperature distribution near the center of the current for the first year of data (site BS3 in Fig. 2). The warm Alaskan coastal water (defined here as $1°C < \theta < 7°C$ and $30.5 < S < 32$) is clearly evident in late summer/early fall of 2002, and again in July 2003 (note that it arrived much earlier the second summer). Another notable aspect of the figure is the deep, warm "spikes" that are prevalent in late fall (but occur at various other times of the year as well). These are the signature of storm events when Atlantic water is upwelled because of strong easterly winds (Münchow et al. 2006; PM). Notably absent from Fig. 3 is a clear signature of the Chukchi/Bering summer water, which is resident over the Chukchi Sea in the late summer months (Coachman et al. 1975). However, in the second year of data this water mass (defined as $-1°C < \theta < 1°C$ and $31 < S < 32.5$) was present in a significant amount in late fall after the passage of the warm Alaskan coastal water

[2] The dominant tidal signals were weak, less than 2 cm s^{-1}.

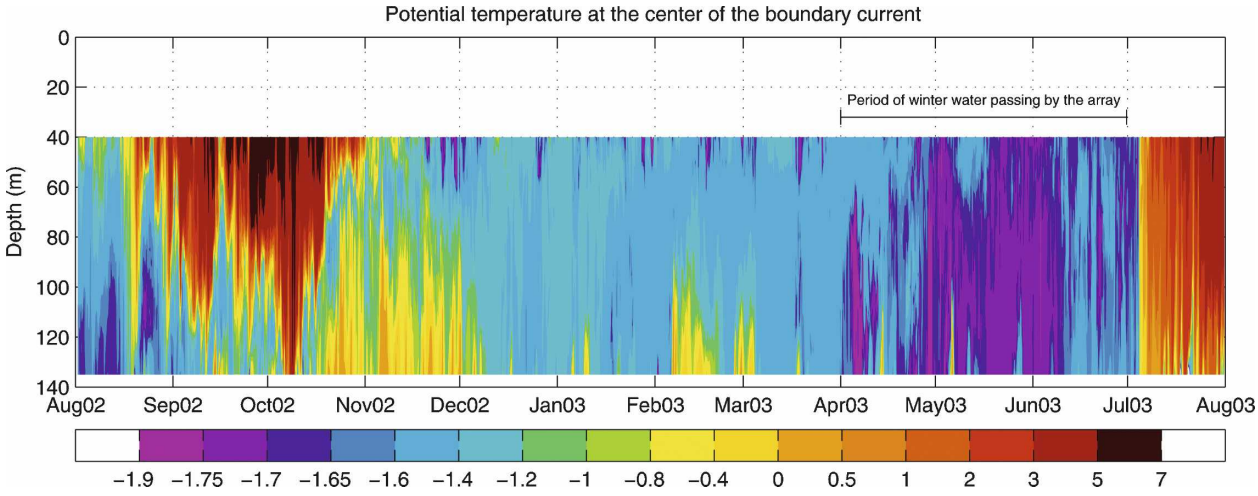

FIG. 3. Time series of potential temperature (°C) at the center of the boundary current (site BS3, see Fig. 2). The 3-month period of focus for this study is indicated.

(attesting to interannual variability of the hydrographic structure of the current).

The period that we are focusing on in this study is the time when the bulk of the coldest Chukchi/Bering winter water flowed by the array. In 2003 this occurred during the months of April–June (Fig. 3) when the temperature was <-1.7°C. Based on θ–S values and nutrient concentrations, this is the same water mass that often occupies the center of cold-core anticyclones observed in the southern Canada Basin (Muench et al. 2000; Pickart et al. 2005; Llinas et al. 2008). Using our vertical sections we constructed time series of the properties of the winter water in the boundary current during this period by integrating the area within the -1.7°C contour for each realization. The salinity of the winter water so computed shows considerable variation over the 3-month period, ranging between 32 and 34 (Fig. 4a). This means that the boundary current is capable of ventilating both the lower and upper halocline.

During the latter half of April the winter water was saltiest, with much of it corresponding to the "cold, hypersaline mode" that Weingartner et al. (1998) observed in the Chukchi Sea. This implies that dense polynya water from the northeast Chukchi shelf can end up in the shelfbreak boundary current. To assess the likelihood of this, we examined ice concentration data from the Advanced Microwave Scanning Radiometer for Earth Observing System (EOS; AMSR-E) for the previous winter. Polynya activity was common along the Alaskan coast from Cape Lisburne to Barrow. During the time period of 1 January–15 April 2003 (which was after freeze up and before melt back), the ice concentration was <65% somewhere along this portion of the coast roughly half the time. From about mid-May onward the winter water measured by the array was significantly less dense and, according to Melling's (1998) definition, was lighter than the upper halocline of the Canadian Beaufort Sea (Fig. 4a). However, this density level is within the lower part of the "summer Pacific halocline" discussed by Steele et al. (2004).

The gray shading in Fig. 4a represents the range in salinity within the patch of water colder than -1.7°C for the collection of vertical sections. At times there is a wide range of winter water present (sometimes spanning the entire halocline, e.g., in mid-April). This is partly due to the amount (cross-sectional area) of winter water contained in the section, which is plotted versus time in Fig. 4b. Note that there are times when greater than 50% of the section (up to 300 m) is occupied by the winter water, although after the first week of June the amount was generally less than 5%. The overall message from Fig. 4 is that, downstream of Barrow Canyon, the boundary current advects the coldest winter water sometime after the conclusion of winter (this was true in the second year of data as well), and that there can be a significant range in the density and amount of winter water during a given year, spanning most of the halocline.

c. *Structure and dynamics*

It is our intent to investigate the variability of the boundary current, and its ability to form eddies, in the absence of external forcing. While the winds over the Chukchi and Beaufort Seas generally weaken in spring, and the frequency of storms decreases, there are still wind events that disrupt the current. Upwelling events tend to reverse the current, and downwelling events

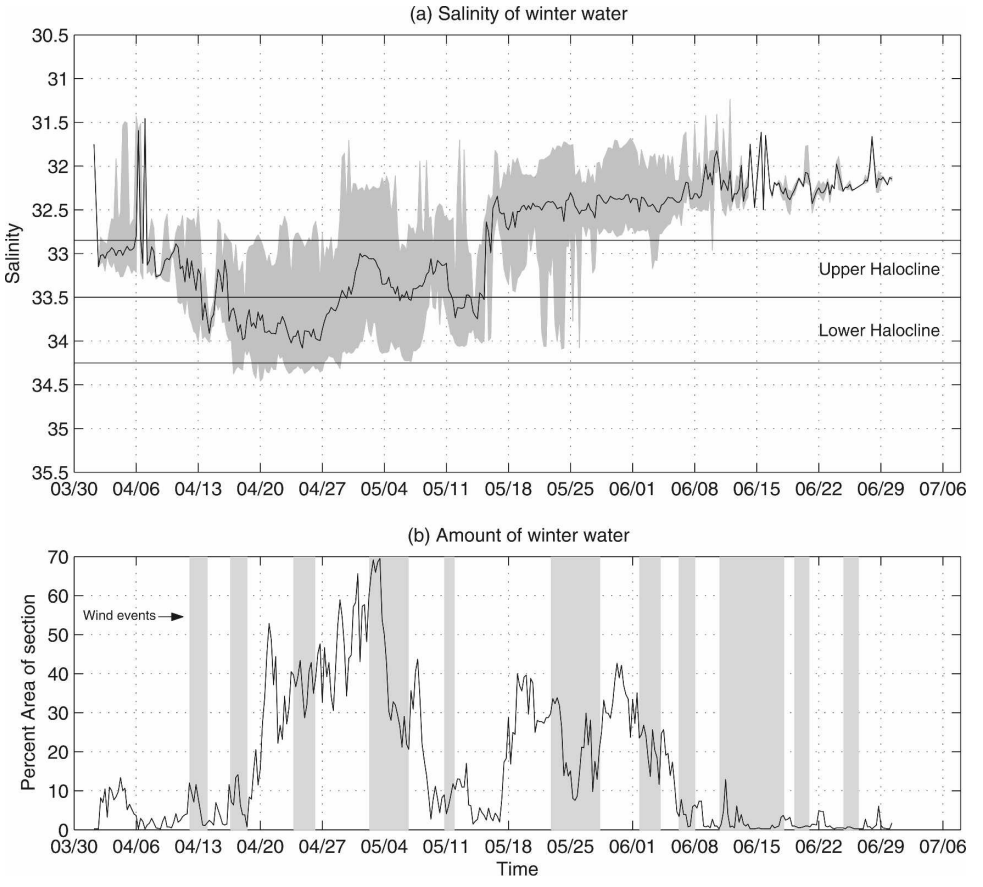

FIG. 4. Properties of the Chukchi/Bering winter water during spring 2003. The winter water is defined as that water colder than −1.7°C. (a) Mean salinity (black line) and range of salinity (gray shading). The limits of the cold halocline based on historical data from the region (Pickart 2004) are shown. (b) Area of the winter water expressed as a percent of the total area of the section to 300-m depth. The periods denoted by gray shading are upwelling events.

enhance it. One can see in Fig. 3 that there were two strong upwelling events during spring 2003 (one in April and one in May). To isolate the time periods when the boundary current was a free jet, we developed an objective procedure for identifying the wind events. Essentially, an upwelling (downwelling) event was identified when the following criteria were met: 1) significant easterly (westerly) winds were measured at the Point Barrow weather station, 2) the dominant flow throughout the section was westward (strongly eastward), and 3) the average near-bottom salinity in the vicinity of the shelf break reached a value well above (below) the mean monthly value, resulting from the upslope (downslope) movement of the water. We used salinity rather than temperature because it increases monotonically with depth (during certain springtime storms cold water was upwelled). Note that our wind filter removes only the synoptic weather events; it is insensitive to the mean, large-scale winds that force the anticyclonic Beaufort gyre circulation.

Using these criteria we identified 10 upwelling events over the time period from April to June (not all of them were strong), which were removed from our collection of sections (Fig. 4b shows these events).[3] Because the hydrographic response to the wind tended to lag the current response, it meant that some velocity sections were removed even though the current was flowing eastward (shortly after the storm ended). In all, 161 realizations, or 44% of the data, were discarded over the 3-month period (there were no downwelling events). This is unfortunate, because among other things it reduces the confidence of the computed statistics, but we are left with no choice in order to isolate the free jet. The well-behaved mean fields and interpretable variability presented below gives us confidence that the remaining 203 realizations provide meaningful results.

[3] An additional current reversal was removed in May despite the presence of weak winds at the time.

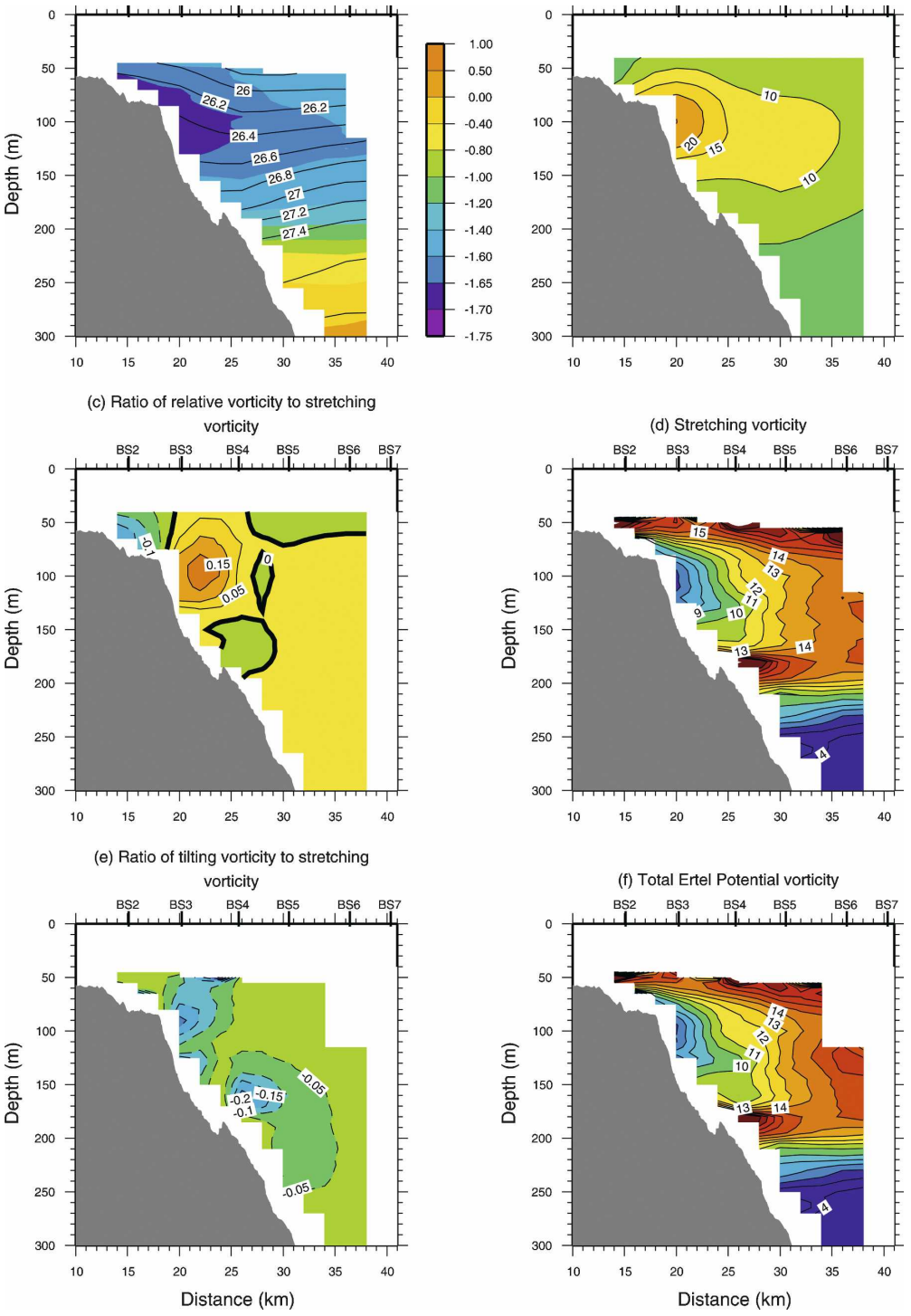

FIG. 5. (a)–(f) Mean vertical sections of the unforced jet.

1) MEAN FIELDS

The mean structure of the free jet is shown in Fig. 5. The presence of the cold winter water is evident at the shelf break (Fig. 5a), coincident with an eastward velocity maximum exceeding 20 cm s^{-1} (Fig. 5b). The mean temperature structure over this time period is quite different from the year-long mean section resulting from the absence of the Atlantic water influence near the shelf break (because the upwelling storms

have been removed). The velocity structure is different as well; the mean unforced jet is 75% stronger than the year-long average flow, and the free jet does not have the deep tail that forms during the winter storm season (see NIK). The transport of the free jet over the 3-month period is 0.42 Sv (1 Sv $\equiv 10^6$ m^3 s^{-1}). This is 3 times larger than the year-long average Pacific water transport of 0.13 Sv (NIK).

The potential vorticity structure of the boundary current provides important insights regarding the dynamics of the flow. For most large-scale ocean currents (and even for many energetic currents), the stretching vorticity is the dominant term in π. Because of the small spatial scales of the high-latitude Beaufort shelfbreak jet, however, one might expect the other two terms to play an important role in the space–time evolution of the current. Figure 5c shows the ratio of the relative vorticity to the stretching vorticity for the mean free jet (same as $-\overline{u_y}/f$). One sees the enhanced cyclonic (anticyclonic) vorticity on the seaward (shoreward) side of the jet, although for the mean current the values are relatively small. The stretching vorticity (Fig. 5d) shows a pronounced minimum at the shelf break associated with the weakly stratified winter water, which was likely formed via convective overturning in the Chukchi Sea. Note the spreading of the 26.2 and 26.6 isopcynals, which bound the mean winter water, as they progress onshore (Fig. 5a). The thermal wind shear associated with this isopycnal spreading dictates the vertical extent of the current, and also gives rise to the two regions of enhanced tilting vorticity above and below the jet (Fig. 5e; note that, for a geostrophic flow, the tilting vorticity is a negative-definite quantity, displayed here as the ratio between the tilting and stretching terms). In the mean, the tilting term is also fairly small (comparable to the relative vorticity).

The average total Ertel potential vorticity is shown in Fig. 5f. For the mean jet it is qualitatively similar to the stretching vorticity. The distribution of π shows a very important feature of the Beaufort shelfbreak jet, namely, that the cross-stream gradient of potential vorticity changes sign with depth. At the depth level of the jet core π increases offshore, from the low values in the winter water to the higher values of the ambient interior water. Below the jet core, the halocline is compressed due to the presence of the winter water pycnostad (note the 27 and 27.2 isopycnals in Fig. 5a), which results in a region of high potential vorticity adjacent to the slope near 180 m. This compression lessens offshore of the winter water, resulting in a decrease of π at this depth level. Such a change in the sign of π_y is a necessary condition for baroclinic instability of the current, which, as seen below, appears to lead to eddy formation. Note that the sloping bottom causes the deeper region of potential vorticity gradient to be offset from the upper region of the potential vorticity gradient, a feature that may play into the stability of the boundary current, as discussed further in section 4c and Spall and Pedlosky (2008).

2) TEMPORAL VARIABILITY

Despite the well-behaved mean fields in Fig. 5, the unforced jet is highly variable in time. This is seen, for example, in Fig. 4b, which shows that the amount of winter water measured by the array changes considerably independent of the wind, on a variety of time scales. To demonstrate this we present a synoptic snapshot of the current in late April, when there was a large amount of winter water present (Fig. 6). Comparing this to the mean state (Fig. 5), one sees that the boundary current can have a significantly different structure instantaneously. In this realization the newly ventilated winter water (colder than -1.75°C) occupies a large part of the slope, and the ispocynals beneath the pycnostad descend downward very sharply (Fig. 6a). The associated thermal wind shear is strong enough to reverse the jet near the bottom (Fig. 6b). The eastward-flowing portion of the jet is >50 cm s^{-1}, with a relative vorticity that exceeds $0.4f$ (Fig. 6c). While the stretching vorticity (Fig. 6d) shows the same feature as the mean, that is, a region of low vorticity associated with the uniform winter water (100–150 m), it also contains low values farther offshore where the isopycnals descend (150–200 m). In fact, the isopycnal slope is so steep there that the tilting vorticity exceeds the stretching vorticity (Fig. 6e). Combined with the negative relative vorticity associated with the deep reversal of the jet, this results in a region of negative Ertel potential vorticity (Fig. 6f; near $x = 30$–35 km). It is clear, therefore, that all three terms of π can be important synoptically in the Beaufort shelfbreak current.

How often is this the case? To answer this we created vertical sections of the ratio $R_{\rm pv}$, defined as the sum of the relative plus tilting vorticity divided by the stretching vorticity. As mentioned earlier, for large-scale flows $|R_{\rm pv}| \ll 1$, and for the mean free jet of Fig. 5 it is small. However, based on Fig. 6 we expect that instantaneously $R_{\rm pv}$ will be significant. For each realization we determined both the positive and negative extrema of $R_{\rm pv}$, and where these values occurred in the vertical plane. Note that negative values of $R_{\rm pv}$ can result from both the tilting vorticity and anticyclonic relative vorticity, whereas positive values are due to cyclonic relative vorticity.

Figure 7a shows a histogram of the extrema of $R_{\rm pv}$ for the 3-month period. The positive values are sharply

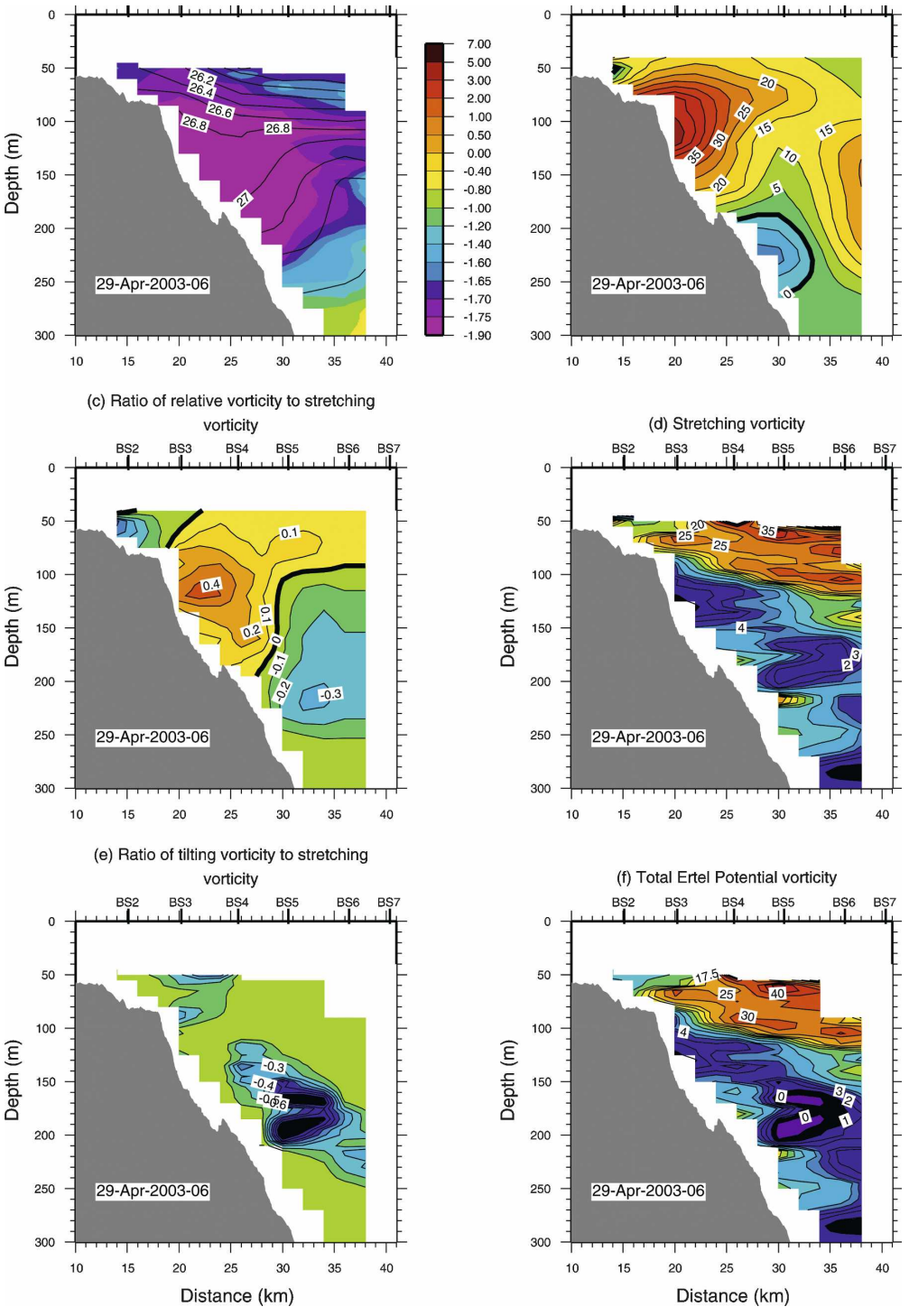

FIG. 6. (a)–(f) Vertical sections of a snapshot of the jet at 0600 UTC 29 Apr 2003.

peaked, with only 3% of the realizations containing $R_{pv} > 0.5$. In contrast, the negative values are broadly distributed over a large range, and more than 70% of the realizations contained $R_{pv} < -0.5$. As seen in the example above (Fig. 6), the deflection of isopycnals resulting from the winter water can be large enough to make the total potential vorticity negative, and Fig. 7a indicates that this happened (i.e., $R_{pv} < -1$) a third of the time during the spring of 2003. Figure 7b shows where the extreme values of R_{pv} occurred in relation to

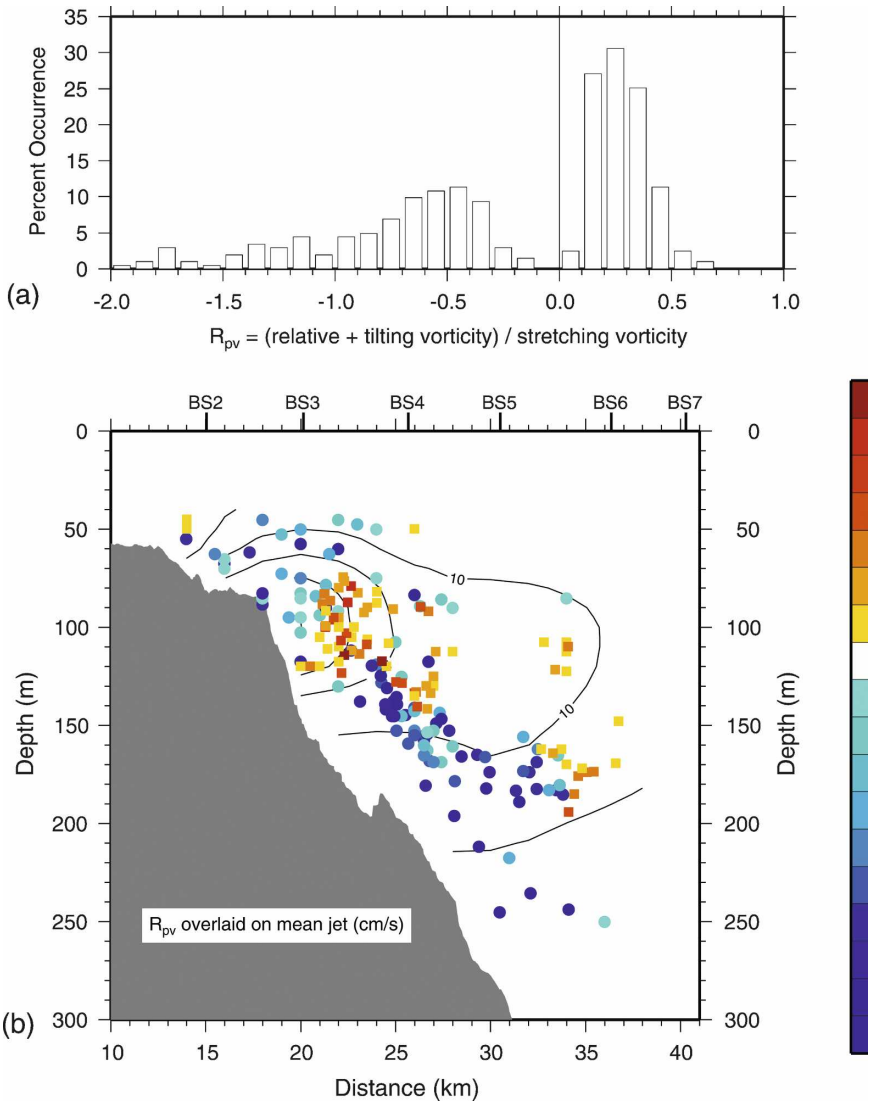

FIG. 7. (a) Histogram of the positive and negative extrema of R_{pv} for the collection of sections. (b) Scatterplot of the extrema of R_{pv} overlaid on the mean along-stream velocity section of Fig. 5.

the mean jet. Consistent with the mean section (Fig. 5), the largest positive values occurred on the seaward side of the jet. There is, however, a second cluster of large positive values well offshore (near $x = 33$ km). These correspond to periods when at least a portion of the jet was detached, or when eddies were passing by the array. The negative values of R_{pv} occur in two general clusters associated with the upward and downward deflection of isopycnals surrounding the winter water pycnostad (this is also consistent with the mean section). Interestingly, the largest negative values occur below the jet, which has strong ramifications for the eddy buoyancy flux and energetics of the current, as discussed later in the paper.

3. An idealized model of eddy formation and ventilation

The observations presented above have motivated us to consider the ability of a middepth boundary current of low potential vorticity water (the Chukchi/Bering winter water) to ventilate the western Arctic halocline through the formation of anticyclonic eddies. The presence of these eddies near the boundary current, in regions away from the two canyon outflows, suggests that they are formed all along the boundary, and that the topography associated with the canyons may be of second-order importance. Our objectives in developing the model are as follows: to explore the efficiency of

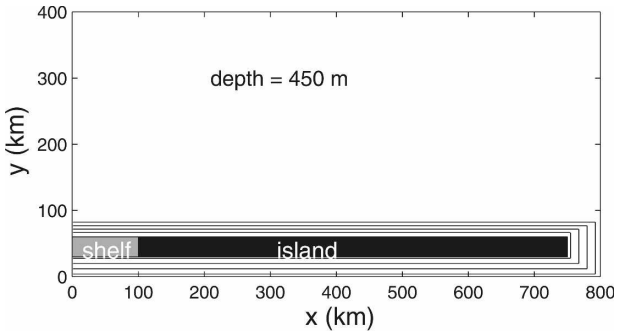

FIG. 8. Model topography (contour interval is 100 m) and domain. The black region is an island; the gray region is a 70-m-deep shelf where the temperature, salinity, and momentum are forced.

eddy formation from such a boundary current, to compare the mean structure and variability of the boundary current and eddies to observations, and to assess the ability of this eddy formation mechanism to play an important role in the ventilation of the western Arctic halocline. Our approach is very idealized, allowing for the determination of the sensitivity of the eddy formations to both physical and numerical parameters. However, the central calculations are carried out in a parameter space that is representative of the observed circulation along the shelf break of the Chukchi and Beaufort Seas.

a. Model configuration

The numerical model used is the Massachusetts Institute of Technology (MIT) general circulation model (Marshall et al. 1997). This model solves the hydrostatic, primitive equations on a uniform Cartesian staggered-C grid with level vertical coordinates. A partial cell treatment of the bottom topography is accurate for steep topography in the presence of stratification, which is expected to be important for the present problem.

The model domain consists of a narrow island with sloping topography extending into deep water, and a shelf region 70 m deep at the western end of the island[4] (see Fig. 8). The topography slopes linearly from 70-m depth to the maximum model depth of 450 m over a horizontal length scale of 19 km, giving a slope of $s = 0.02$ (this will be varied in section 4c). The land area is indicated by black. The horizontal resolution is 1 km and there are 27 levels in the vertical with 10-m spacing between 0- and 220-m depth and from 30- to 50-m spacing between 220 and 450 m. Because we are interested in the boundary current structure and eddies that exist within the halocline, the model domain is limited to the upper ocean. The initial stratification for temperature and salinity are uniform and taken from the May monthly mean version 3.0 Polar Science Center Hydrographic Climatology (PHC3.0; updated from Steele et al. 2001) at 74°N, 150°W.

The model incorporates second-order vertical viscosity and diffusivity with coefficients of 10^{-5} m^2 s^{-1}. The vertical diffusion is increased to 1000 m^2 s^{-1} for statically unstable conditions in order to represent vertical convection. Horizontal viscosity is parameterized as a second-order operator with the coefficient A_h determined by a Smagorinsky (1963) closure as

$$A_h = (\nu_s/\pi)^2 L^2 D. \tag{2}$$

Here, ν_s is a nondimensional coefficient taken to be 1, L is the grid spacing, and D is the deformation rate, defined as

$$D = [(u_x - v_y)^2 + (u_y + v_x)^2]^{1/2}, \tag{3}$$

where u and v are the resolved horizontal velocities and subscripts indicate partial differentiation. The deformation rate is typically dominated by the lateral shear, which can vary from $O(10^{-5}$ s$^{-1})$ for eddies in the interior to $O(10^{-4}$ s$^{-1})$ for the no-slip shear layer between the shelfbreak jet and the boundary. For the grid spacing of 1 km, this gives a range of lateral viscosity between 1 and 10 m^2 s^{-1}. Sutyrin (1992) has shown that this form of momentum mixing results in the weaker decay of isolated vorticies than does uniform lateral viscosity.

The model is forced by generating dense water over a 100-km portion of the shelf in the western part of the domain (region of gray shading in Fig. 8) and advecting this water toward the shelf break. The water mass properties (temperature and salinity) and a barotropic northward flow are forced through the addition of restoring terms to the temperature, salinity, and meridional momentum equations. The restoring time scale is 1 h and is applied only within the gray-shaded region. Salinity is restored toward 30.5, 31.25, 32.0, 32.5, 32.5, 32.5, and 32.5 over the seven model levels over the shelf. Temperature is restored toward −1.8°C, and the meridional velocity toward 7.5 cm s^{-1} for the 70-m shelf depth. In addition, the model temperature and salinity are restored toward the initial climatological stratification within 50 km of the eastern and northern boundaries of the domain with a time scale of 5 days. This suppresses baroclinic Kelvin waves that are generated where the dense waters interact with the solid boundary

[4] Although all calculations here are on an f plane, we refer to the direction increasing toward deep water as north and the direction along the island toward the right as east.

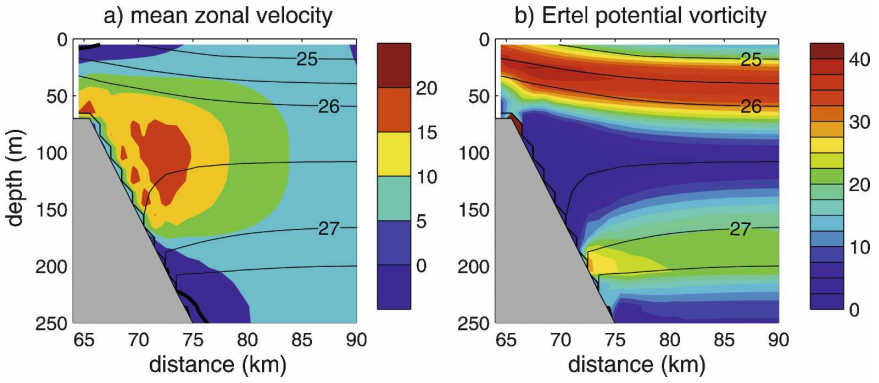

FIG. 9. Meridional section of the mean boundary current (a) zonal velocity (cm s^{-1}) and (b) Ertel potential vorticity (10^{-9} m^{-1} s^{-1}). Isopycnals are indicated by the black contours.

at the eastern end of the island and prohibits these waves from returning to the shelf region and contaminating the intended outflow. The model calculates density from a linear equation of state as

$$\rho = \rho_0 + \beta(S - S_0) - \alpha T, \tag{4}$$

where $\beta = 0.8$ Kg m^{-3} and $\alpha = 0.04$ Kg m^{-3} °C^{-1} are the haline and thermal expansion coefficients, respectively, $\rho_0 = 1026.5$ Kg m^{-3} is a reference density, and $S_0 = 32.5$ is a reference salinity.

The model formulation is intended to represent the eastward flow of Pacific-origin winter water along the shelf break of the Chukchi and Beaufort Seas. The data described in section 2 and in Pickart et al. (2005) suggest that eddies are formed all along the shelf break and are not confined only to the areas in the vicinity of Herald and Barrow Canyons. Although some previous modeling studies have considered the flow in the vicinity of such canyons (e.g., D'Asaro 1988a; Chao and Shaw 2003b), the focus of this study is on the stability of the boundary current away from these relatively small-scale topographic features.

There are several advantages to this formulation. The northward transport is provided by water flowing anticyclonically around the island, and thus avoids the need for open boundary conditions. In addition, the structure of the boundary current is not specified, but instead develops naturally as part of the solution. The stability of the boundary current is very sensitive to its potential vorticity structure and we wanted to avoid specifying this as an initial condition because this would directly control the outcome of the simulation. This approach also provides a continual source of kinetic and potential energy for the boundary current and thus avoids the spin down that is inherent in periodic domain calculations of unstable currents. This idealized approach also allows us to explore the sensitivity of the eddy formation process to environmental parameters, such as the bottom slope, and physical processes, such as ice-induced drag and lateral friction.

The Arctic Ocean is ice covered for much of the year near its margins, and year-round in the interior. It has been speculated that drag induced by the ice cover is important for the long-term evolution of eddies in the Arctic interior (Ou and Gordon 1986; Chao and Shaw 1996). To represent this stress, a quadratic drag law has been applied to the uppermost model level with the coefficient $C_D = 2 \times 10^{-4}$. This gives a spindown time scale of $\tau = H/C_D U^2$, which, for a thickness of $H = 50$ m and a horizontal velocity of $U = 10$ cm s^{-1}, gives $\tau \approx$ 25 days. This will dampen near-surface velocities on the order of the boundary current strength fairly quickly compared to the estimated lifetime of the eddies in the absence of ice (note that this damping will have little impact on the anticyclonic eddies centered near 100-m depth). This calculation has no bottom drag, and the addition of bottom drag does not change the mean current or energetics of eddy formation significantly.

The model is run for a period of 180 days. It takes about 40 days for the outflow from the model shelf to reach the eastern end of the island. The analysis in this section will focus on the mean and eddy variability of this central calculation, while the dynamical processes involved in the eddy formation and its sensitivity to model configuration and parameters will be discussed in the following section.

b. Mean boundary current

The vertical structure of the mean boundary current is shown in Fig. 9, averaged over the final 100 days of integration and between 100- and 700-km longitude. The zonal flow is subsurface intensified with a maximum mean velocity of $O(25$ cm $s^{-1})$. The maximum velocity is located several kilometers offshore of the

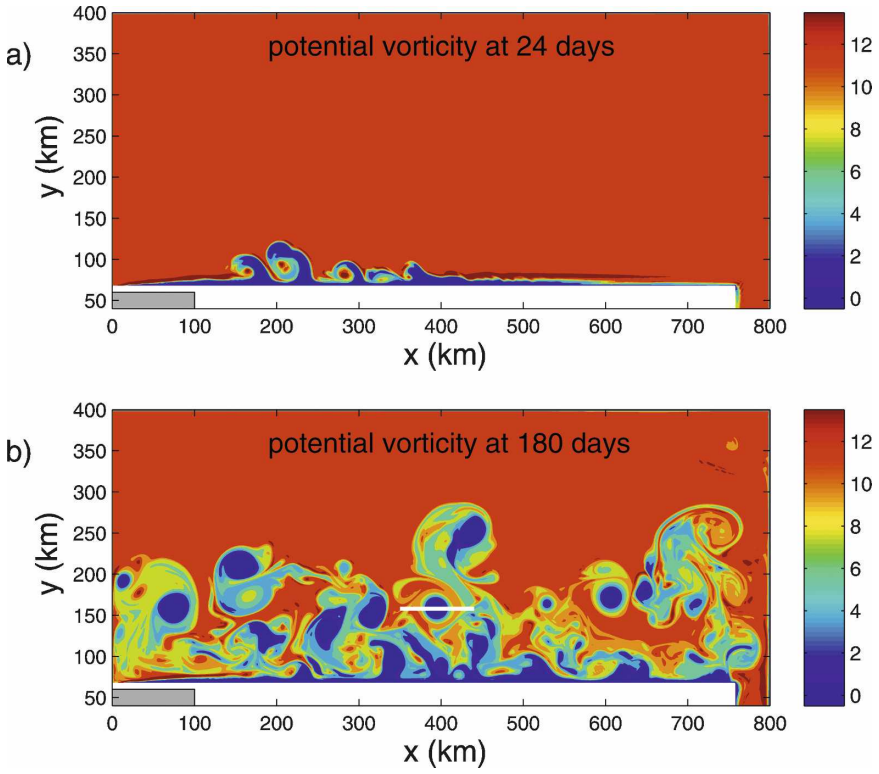

FIG. 10. Potential vorticity (10^{-9} m^{-1} s^{-1}) at 115-m depth on (a) day 24 and (b) day 180. The white line in (b) marks the location of the vertical section in Fig. 11

sloping bottom, reflecting the no-slip lateral boundary conditions in the model. The net eastward transport is 0.37 Sv, similar to the mean transport of 0.42 Sv calculated from the mooring array during periods of weak winds.

The salinity within the eastward-flowing boundary current is nearly uniform with a value close to 32.5, the same as the waters advected off the shelf at the western end of the island. The shallow isohalines slope upward toward the boundary, consistent with the mooring data presented above and with climatological observations (Pickart 2004). The deep isohalines slope downward toward the boundary, resulting in a spreading of the isopycnals toward the boundary. This is the result of the low potential vorticity in the core of the shelfbreak jet instead of downslope advection in a bottom boundary layer because this calculation has no bottom drag. Thermal wind balances the eastward-flowing middepth maximum boundary current. The Ertel potential vorticity (1) is shown in Fig. 9b. Because of the very weak stratification on the shelf where the boundary current waters originated, the boundary current water has potential vorticity close to zero. There is a band of high potential vorticity in the upper 50 m over the jet, which results from the outcropping isopycnals and enhanced stratification. There is also a region of enhanced potential vorticity near 200-m depth, where the downward-sloping isopycnals intersect the bottom. This general pattern is consistent with the mooring data (Fig. 5). The lateral gradient of potential vorticity is positive at middepth and negative in both the upper and lower portions of the boundary current, consistent with the mooring data and suggestive of baroclinic instability. There is a weak minimum of potential vorticity in the basin interior at approximately 120-m depth, close to the depth of the low potential vorticity boundary current water. This minimum is found in the PHC climatology, and is perhaps reflective of the transport of weakly stratified shelf-origin waters offshore.

c. *Ventilation by anticyclonic eddies*

As time progresses in the model simulation, the boundary current becomes unstable and sheds numerous middepth, anticyclonic, low potential vorticity eddies into the basin interior. After 24 days, the low potential vorticity waters have penetrated 500–600 km eastward along the sloping bottom (see Fig. 10a). A series of meanders has developed and, in some cases, narrow filaments of low-π water are extending into the interior. The relative vorticity within these filaments is

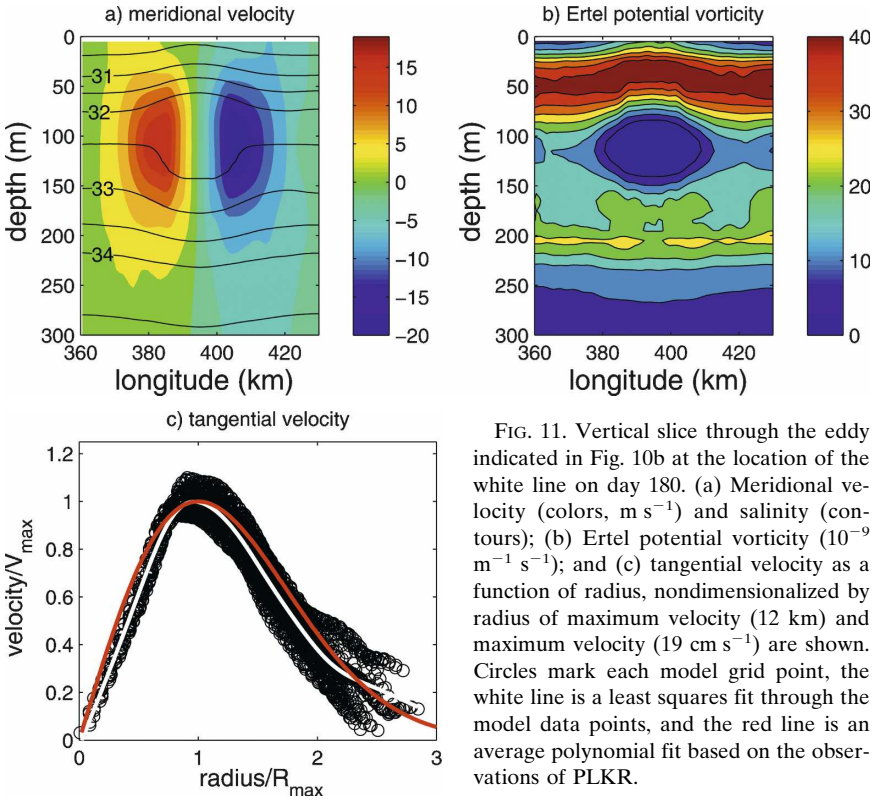

FIG. 11. Vertical slice through the eddy indicated in Fig. 10b at the location of the white line on day 180. (a) Meridional velocity (colors, m s^{-1}) and salinity (contours); (b) Ertel potential vorticity (10^{-9} m^{-1} s^{-1}); and (c) tangential velocity as a function of radius, nondimensionalized by radius of maximum velocity (12 km) and maximum velocity (19 cm s^{-1}) are shown. Circles mark each model grid point, the white line is a least squares fit through the model data points, and the red line is an average polynomial fit based on the observations of PLKR.

anticyclonic and the relative vorticity between the filaments is cyclonic. The initial meander development is characterized by a dipole pair, or heton (Hogg and Stommel 1985), with a middepth anticyclone and a shallow cyclone slightly offset in the upstream direction. The cyclones are composed of ambient waters from the interior, and thus do not contain an anomalous potential vorticity or tracer signal. They are most evident in the pressure and velocity field, although filaments of low-π boundary current water often get wrapped around their perimeters during the formation process, making them identifiable in the tracer field as well. This configuration is typical of what is found for unstable currents (Pedlosky 1985; Spall 1995; Bush et al. 1996; Shimada and Kubokawa 1997) and is very effective at transporting tracers away from the front. After 180 days (Fig. 10b), the model has formed numerous low-π, anticyclonic eddies that have propagated well into the basin interior. They are formed all along the boundary, beginning just downstream from the shelf region where the model is forced. The eddies vary in size but are typically 30 km in diameter, with cores of nearly uniform, very low potential vorticity. The upper ocean cyclonic partners that had originally formed along with these middepth anticyclones have decayed as a result of the quadratic drag applied to the surface layer, parameterizing stress induced by interactions with the ice [consistent with the results of Chao and Shaw (1996)].

A vertical section on day 180 through the low-π eddy located near 400-km longitude and 160-km latitude is shown in Fig. 11. This eddy was formed around day 60, propagated as far north as 300-km latitude, and then moved back toward the shelf. The velocity is anticyclonic throughout the upper 300 m with maximum velocities of O(20 cm s^{-1}). The salinity shows the weak stratification in the core of the eddy, with a doming of isohalines above and a deepening of isohalines below the core of the eddy. The potential vorticity field reflects this low-π core. Note that the anomalous potential vorticity signal is confined to the density range of the anomalous source waters, located between 90 and 150 m. The velocity signal extends over a larger range of the water column because the waters both above and below the low-π core of the eddy are compressed as the weakly stratified core of the eddy passes by. This compression of the water column forces an anticyclonic circulation in order to conserve potential vorticity (Spall 1995).

Figure 11c shows tangential velocity versus radius at a depth of 115 m for the eddy shown in the vertical slice in Figs. 11a,b. The tangential velocities at each model grid point are indicated by the black symbols, and the

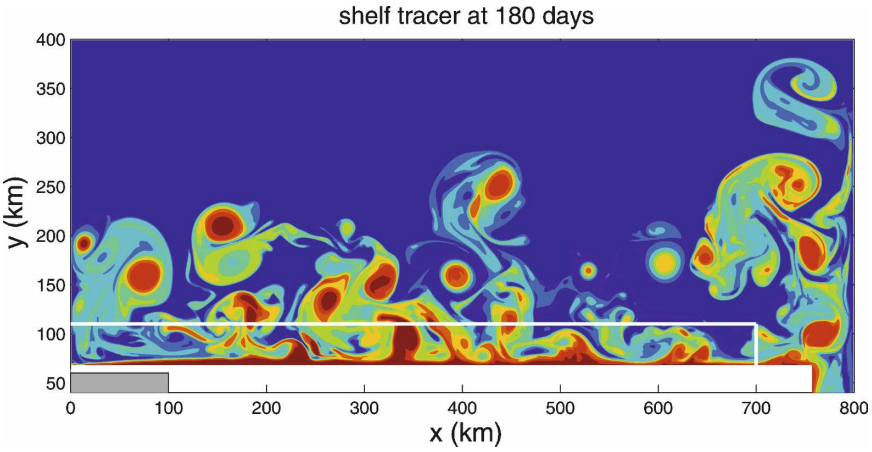

FIG. 12. Passive tracer in the model on day 180 at 115-m depth. The region of offshore and alongshore tracer flux is indicated by the bold white lines. The tracer is initially zero everywhere in the domain, maintained at a value of 1 in the shelf forcing region, and is otherwise advected and diffused as temperature and salinity.

white line is a cubic spline fit to the model data points. The velocity has been scaled by the maximum of the spline fit profile (V_{max} = 19 cm s^{-1}) and the radius has been scaled by the radius of this maximum tangential velocity (R_{max} = 12 km, where $V = V_{max}$). The degree to which the eddy is radially symmetric is evident in the scatter of the individual model grid points. The eddy core ($r < R_{max}$) shows relatively less scatter and is consistent with solid-body rotation. The region of velocity decay ($r > R_{max}$) shows increasing variability with increasing distance from the eddy center.

The velocity magnitude and radial structure of the model eddy are consistent with that observed from drifting platforms. Direct current observations reported by Manley and Hunkins (1985) indicate values of V_{max} from 30 to 50 cm s^{-1}. D'Asaro (1988b) reports V_{max} from 10 to 30 cm s^{-1} for three different halocline anticyclones; PLKR report statistics from 29 eddy encounters, where the mean V_{max} was 24 cm s^{-1}. Thus, the strength of the model eddy (V_{max} = 19 cm s^{-1}) is representative of, although perhaps slightly weaker than, the typical observed eddy. The model produces eddies that range in radius from approximately 5 to 20 km, but all show a similar velocity profile when scaled the same way.

Despite many Arctic eddy observations, reports of tangential velocity versus eddy radius, passing from near the eddy center through the radius of maximum velocity, are relatively rare. Where radial structure has been reported (Newton et al. 1974, D'Asaro 1988b; Timmerman et al. 2008), it is consistent with a solid-body core and a decay region of about 1.5 times R_{max}. Observations from ADCPs on ice-tethered drifters (PLKR) were used to produce a normalized radial structure for comparison with the model eddy. Velocity data from 29 eddy encounters that clearly passed into the solid-body core were rotated into radial and tangential components using an estimated eddy center, and a third-order polynomial fit was made assuming $V = 0$ at $R = 0$. Tangential velocity and radius from the fits were then scaled in the same manner as described above for the model eddy. The average of the normalized radial structure from the polynomial fits is shown in Fig. 11c (red line), and compares very well with the radial average structure of the model eddy. The observations indicate a self-similar structure for the 29 eddies, with typical values in strength of 20–35 cm s^{-1} and in size from 2 to 9 km. Although the model eddies are somewhat larger and weaker, the good agreement in the normalized radial structure with the observations is encouraging.

The anticyclonic eddies in the model transport waters that originated on the shelf into the basin interior. This is evident from the salinity and potential vorticity signals in the core of the eddies. A passive tracer has been added to the calculation in order to quantify the offshore transport by the eddies. This tracer is advected and diffused in the same way as are temperature and salinity, but is initialized at zero throughout the domain and maintained at a value of 1 within the forcing region on the shelf. A plan view of the tracer on day 180 at a depth of 115 m is shown in Fig. 12. The tracer clearly marks the location of the boundary current and core of the offshore eddies. The offshore flux of boundary current water, normalized by the flux off the shelf, is quantified by integrating the tracer flux as

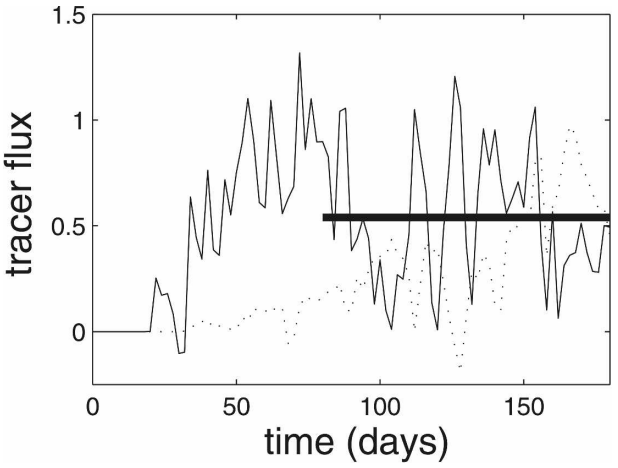

FIG. 13. The offshore (solid line) and alongshore (dashed line) advective flux of the passive tracer as a function of time, normalized by the flux of tracer off the shelf in the forcing region. The mean offshore tracer flux over the final 100 days of integration is indicated by the bold line (53%).

$$F = \frac{\int_0^X \int_0^H v(y_0) T_p(y_0)\, dz\, dx}{\int_0^{X_s} \int_0^H v(y_s) T_p(y_s)\, dz\, dx}, \tag{5}$$

where T_p is the passive tracer, H is the bottom depth, v is the meridional velocity, $X = 700$ km is the zonal extent of the integral for the offshore flux, $X_s = 100$ km is the eastern end of the shelf region, $y_s = 60$ km is the northern limit of the island, and $y_0 = 110$ km is the latitude where the offshore flux is calculated. A similar calculation is applied along a meridional section at $x = X$ between $y = y_s$ and $y = y_0$ to calculate the amount of tracer that is carried out of the region in the boundary current. The offshore and eastern locations of the flux calculation are indicated in Fig. 12 by the white lines. The offshore and alongshore fluxes are shown in Fig. 13 as a function of time. The offshore flux averaged between day 80 and 180 is 53% of the flux off the shelf (indicated by the bold line). The flux is always offshore, but it is characterized by strong, high-frequency events resulting from individual eddy formations. The average of the sum of the alongshore flux and the offshore flux accounts for 93% of the flux off the shelf over this same time period, so there is little temporal storage within the integration contour on these time scales; however, there can be significant storage on synoptic time scales. The offshore and alongshore fluxes are also generally out of phase, indicating that the offshore flux occurs at the expense of the alongshore flux, even on synoptic time scales. Thus, the eddies are capable of transporting a significant amount of the shelf water into the basin interior.

4. Discussion

The standard model configuration presented above develops a middepth, low potential vorticity boundary current that readily forms anticyclonic eddies, which ventilate the interior with shelf water. The mean structure of the model boundary current compares well with the free-jet configuration of the Beaufort shelfbreak jet obtained from the mooring data, and the eddies that it spawns have similar structures to those observed in the southern Canada Basin from drifting platforms. In this section, the mechanisms of the boundary current instability, its impact on the large-scale circulation and boundary current transports, and its sensitivity to model parameters are explored.

a. Energetics

1) MODEL BOUNDARY CURRENT

The source of the boundary current instability is indicated by the terms that convert mean energy into eddy energy. The conversion from mean potential energy into eddy energy is often related to baroclinic instability and is given by

$$\mathrm{BC} = -g\gamma\overline{v'\sigma_\theta'}/\rho_0, \tag{6}$$

where an overbar indicates the time mean, the primes indicate deviations from the time mean, $\gamma = \partial z/\partial y$ is the mean isopycnal slope, and ρ_0 is a reference density. Potential energy is extracted from the mean flow by eddies transporting density down the mean density gradient. The cross-stream eddy density flux $\overline{v'\sigma_\theta'}$ calculated over the final 100 days of integration and then averaged between 100 and 700 km is shown in Fig. 14a, superimposed on the mean density field. There is a positive density flux in the upper 100 m beginning on the offshore side of the mean boundary current and extending into the basin interior. Beneath this, deeper than 100 m, is a similar negative eddy density flux. This is the signal of eddies transporting water of the shelf origin offshore into the stratified interior. The weak decay of the eddy density flux offshore of the maximum is a result of the eddies remaining as coherent features that transport temperature and salinity into the interior.

The BC energy conversion calculated using this eddy density flux and the mean density field is shown in Fig. 14b. A positive value indicates that energy is being extracted from the mean by the growing eddies. The primary regions of energy conversion are centered on the

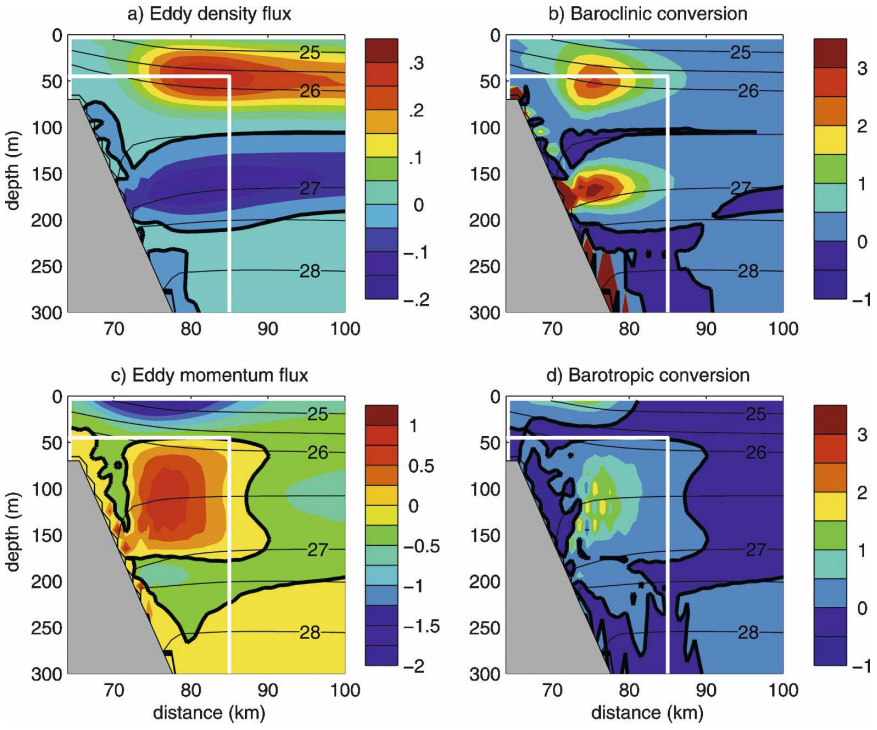

FIG. 14. Along-shelf and temporal mean of the (a) offshore eddy density flux (kg m^{-2} s^{-1} × 10^{-2}), (b) baroclinic energy conversion term (m^2 s^{-3} × 10^{-8}), (c) eddy momentum flux (m^2 s^{-2} × 10^{-3}), and (d) barotropic energy conversion term (m^2 s^{-3} × 10^{-8}), overlaid on the mean density field (thin black contours). The zero contour of each field is given by the bold black line. The white line indicates the region of overlap with the observations (Fig. 15).

sloping isopycnals near 50- and 150-m depth on the offshore side of the boundary current, that is, where the isopycnals spread resulting from the shelf water pycnostad on the slope (Fig. 9b). It is important to note that the energy conversion is limited to the region of sloping isopycnals even though the eddy density flux continues far offshore.

The conversion from mean kinetic energy into eddy energy is related to barotropic instability and is given by

$$\mathrm{BT} = \overline{v'u'}U_y, \tag{7}$$

where U is the time mean zonal velocity. Kinetic energy is extracted from the mean flow by eddies transporting zonal momentum down the mean velocity gradient. The eddy momentum flux $\overline{v'u'}$ calculated over the final 100 days and then averaged between 100 and 700 km is shown in Fig. 14c. The maximum signal is centered near 100-m depth and extends approximately 20 km offshore. The sense of the eddy momentum flux is such that zonal momentum is transported offshore, leading to an offshore shift in the location of the boundary current. This is consistent with the offshore shift of the depth-integrated transport streamfunction as the flow moves eastward along the island (discussed below). The change in zonal momentum that would result from this magnitude of eddy momentum flux divergence, over the zonal extent of the island with mean boundary current strength of 10 cm s^{-1}, is $O(10\ \mathrm{cm\ s^{-1}})$. This would cause the mean flow onshore of the maximum eddy momentum flux to decrease by this amount and the mean flow offshore of the location of the maximum to increase by this amount, which is again consistent with the offshore shift found in the model.

Unlike the eddy density flux, which decays only weakly offshore of its maximum (Fig. 14a), the eddy momentum flux decreases rapidly in the meridional direction, resulting in weakly negative momentum flux offshore of the mean boundary current location (Fig. 14c). This means that while salinity (and other tracers) is carried far from the boundary by the eddies, momentum is not. Hence, the volume transport of the boundary current remains essentially trapped near the boundary, even as the tracers originally within the current are carried far offshore. Because of the symmetry of the eddies, it is clear that they cannot transport momentum but, because of the antisymmetry in density of the baroclinic eddy pairs, they are very effective at transporting density. The eddies are only able to transport momen-

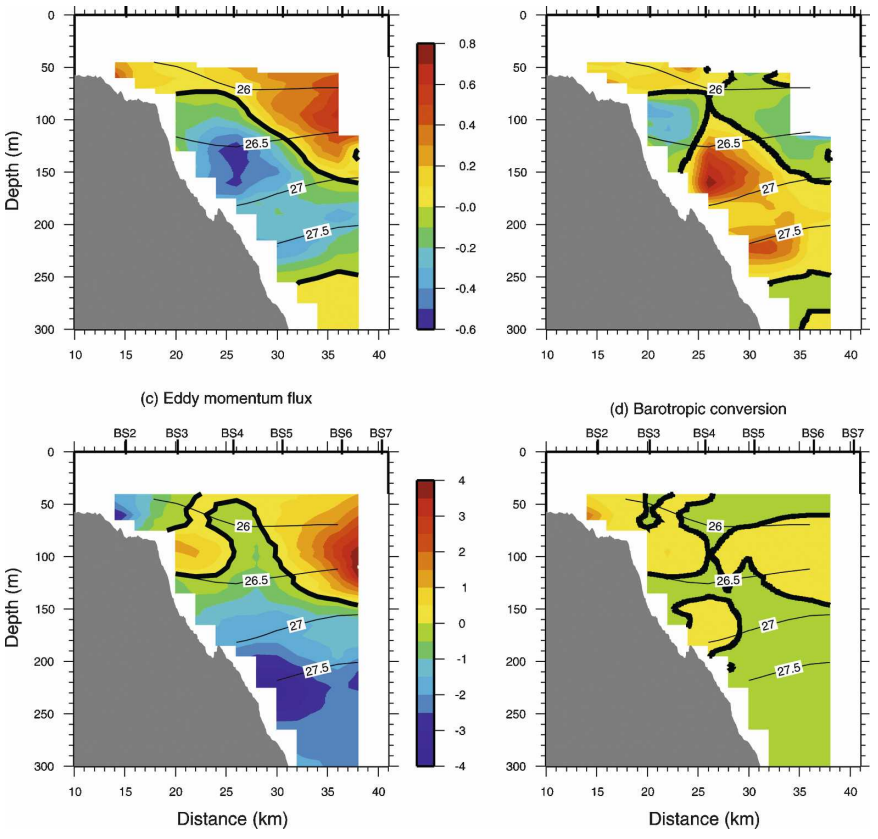

FIG. 15. Results from the mooring data for the (a) offshore eddy density flux (kg m^{-2} s^{-1} × 10^{-2}), (b) baroclinic energy conversion term [(6); m^2 s^{-3} × 10^{-8}], (c) eddy momentum flux (m^2 s^{-2} × 10^{-3}), and (d) barotropic energy conversion term [(7); m^2 s^{-3} × 10^{-8}].

tum during their growth phase, not after they have separated from the mean current, which explains why the current remains close to the boundary.

The energy conversion from the mean kinetic energy to eddy energy is shown in Fig. 14d. The current is also barotropically unstable, with the main region of energy conversion near the core of the boundary current at the depth of weakest stratification. There is also a region of weak energy conversion near the surface. The sense of the middepth conversion is to extract energy from the mean, although the integrated conversion over the entire section is about an order of magnitude less than the integrated baroclinic conversion term. Therefore, the instability of the model boundary current is most aptly described as a baroclinic instability.

2) MEASURED BOUNDARY CURRENT

The eddy fluxes of density and momentum, and the baroclinic and barotropic conversion terms, were also calculated from the mooring data. The mooring array does not extend as far offshore or as shallow in the water column, but the measurements do cover the core of the jet and allow for some comparisons with the energetics in the model. (The approximate region where the data and model overlap is indicated by the white lines in Fig. 14.) As in the model, the observed eddy density flux is positive in the upper portion of the shelfbreak jet and negative in the lower portion, although the zero line is tilted upward toward the boundary in the data whereas the transition from positive to negative is at the middepth of the model jet (Fig. 15a). The magnitude of the flux calculated from the data is similar to that produced in the model. The observed baroclinic conversion term is strongly positive beneath the jet where the isopycnals slope downward (near 150 m; see Fig. 15b). This is consistent with the model also and indicates the conversion from mean potential energy into eddy energy. There is, however, a second area of strong baroclinic conversion in the model above the jet where the isopycnals slope upward (near 60-m depth), which is difficult to resolve conclusively in the observations (although the measured conversion does become positive again at these depths, and data shallower than 40 m are not available).

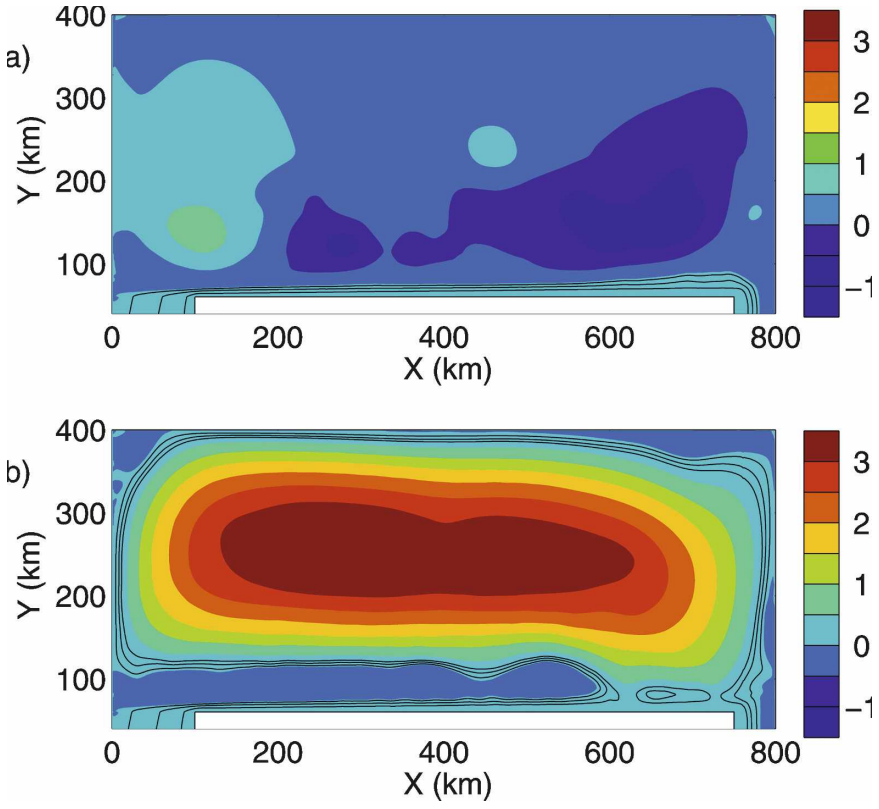

FIG. 16. Mean depth-integrated transport streamfunction (10^6 m s^{-1}) for (a) the standard calculation and (b) a calculation with forcing on the shelf and anticyclonic wind stress curl in the interior. The transport off the shelf is indicated by the black contours (contour interval is 0.1×10^6 m s^{-1}).

The observed eddy momentum flux is mostly positive in the upper 150 m with the maximum located at the offshore limit of the array, approximately 20 km from the shelf break. The magnitude is similar to that found in the model, although the maximum in the model is located closer to the topography. The data also show a strong negative eddy momentum flux below the mean jet, centered at 230 m in a region of weak mean horizontal velocity shear. While the momentum flux in the model is negative at this depth as well, the value is close to zero. Both the data and model have positive barotropic conversion of similar magnitude near the depth of the jet (details of the distribution vary), indicating energy transfer from the mean kinetic energy to eddy energy. Integrating over the entire section, the observed baroclinic conversion is an order of magnitude larger than the barotropic conversion, which was the case in the model as well. Overall then, despite some detailed differences between the model and data, the general patterns and strengths of the eddy fluxes and energy conversion are comparable. This strongly supports the conclusion that the anticyclones observed in the interior of the southern Canada Basin originate from the shelfbreak jet, and that they are formed primarily by baroclinic instability all along the boundary.

b. *Mean transport streamfunction*

The mean depth-integrated transport streamfunction over the final 100 days of integration is shown in Fig. 16a. The circulation is dominated by an eastward flow along the north side of the island and a cyclonic circulation over much of the interior. The circulation around the island is initiated by the northward flow off the shelf between 0- and 100-km longitude. As this dense water flows over deeper topography, the influence of rotation deflects the current toward the right, along the sloping bottom. As mentioned earlier, the total transport off the shelf is approximately 0.37 Sv. The off-shelf transport is indicated in Fig. 16a by the black contours originating on the shelf and turning sharply to the right, west of 100-km longitude. This flow remains close to the boundary, although it moves toward deeper water and broadens slightly as it flows eastward along the sloping bottom. This is consistent with the divergence of the

eddy momentum flux discussed above. The circulation just offshore of the boundary current is primarily cyclonic and of basin scale in the zonal direction. The circulation farther in the interior is both cyclonic (most of the domain) and anticyclonic (around the isolated eddy near 100- and 150-km longitude).

The year-long eastward transport of the Beaufort shelfbreak jet at the array site (Fig. 1) is 0.13 Sv (NIK). This is less than 20% of the long-term transport of Pacific water through the Bering Strait (0.8 Sv; see Roach et al. 1995), and suggests that most of the Pacific water entering the Arctic does not end up in the boundary current east of Barrow Canyon. Even considering periods of weak winds in spring, the focus of this paper, the along-shelf transport is still only $O(50\%)$ of the Bering Strait transport. As described above, our central model calculation shows a slight offshore shift of the eastward boundary current transport, but actually produces an enhanced eastward transport compared to what flows off the shelf. This would seem to be at odds with the mooring data. To investigate this, an additional calculation was carried out in which a wind stress with anticyclonic curl was applied to the basin interior, defined as

$$\tau^x = -\tau_0 \cos[\pi(y - y_s)/(y_n - y_s)], \tag{8}$$

where $\tau_0 = 0.005$ N m^{-2} and y_n is the northern latitude of the domain. This magnitude of wind stress was chosen to give a mean wind-driven circulation in the basin interior of $O(4$ cm s$^{-1})$, consistent with the strength of the anticyclonic Beaufort gyre (Plueddemann et al. 1998). We are considering here only the large-scale mean winds and do not include synoptic storm events related to Aleutian lows originating in the North Pacific. The vorticity input by the wind is dissipated through quadratic bottom friction with the coefficient $C_D = 10^{-3}$. This does not significantly influence the boundary current structure or eddy formations, but it is necessary for balancing the vorticity input by the wind.

The mean transport streamfunction for this wind-driven calculation is shown in Fig. 16b. The interior circulation is now anticyclonic, as expected from the wind forcing. However, the transport near the sloping topography is now eastward only over the shallow topography. As the boundary current water is shifted offshore because of the eddy momentum flux, it becomes entrained into the westward-flowing wind-driven gyre. The gyre is sufficiently strong that it is able to reverse the direction of flow, and with it carry the boundary current water toward the western basin. This is evident by the black contours marking the shelf water transport in Fig. 16b. By approximately 600-km longitude, essentially all of the shelfbreak jet transport has been lost to the basin interior. The region of eastward eddy-driven flow in the southern interior (Fig. 16a) is also competing with the westward wind-driven flow, so that in the wind-driven case there is a broad region of weak mean flow offshore of the boundary current, between approximately 50- and 125-km latitude. The mean transport streamfunction found for the wind-driven case is very similar to what is found if the transport for the central calculation with no wind is simply added to the transport for a wind-driven flow with no dense water outflow.

Hence, the slight offshore diversion of the shelfbreak jet driven by the eddy fluxes, interacting with the interior wind-driven gyre, results in a major transport loss of the boundary current. The loss of transport is fairly abrupt in this calculation, but we expect that time-dependent wind forcing and variability in the source water transport and properties would result in an average loss of transport that is more broadly distributed along the boundary. We note that the year-long mooring deployed near the Mackenzie shelf break (roughly 800 km east of Barrow Canyon) measured mean flow to the west, at a depth where one might expect to see the eastward-flowing boundary current (Kulikov et al. 1998). While not conclusive, this is consistent with the idea of reduced eastward flow at such distances from the Chukchi shelf source. The main point here, however, is that the shelfbreak current can interact with the interior circulation to result in a fundamentally different transport of the shelf waters.

The eddies form in the wind-driven calculation much like they did in the central calculation, although the eddies are advected toward the interior and west by the model Beaufort gyre, as seen by the passive tracer field on day 180 in Fig. 17. This is consistent with the pathways of Bering summer water inferred from observations by Shimada et al. (2001). The spatial distribution of eddies away from the boundary current is significantly different for the wind-driven case (Fig. 17) compared to the standard case (Fig. 12). The wind-driven case is distinguished by a relative scarcity of isolated anticyclones in the eastern half of the domain and a concentration in the west, with many of the western eddies well offshore of the boundary current. The eddy distribution observed from drifting platforms is generally consistent with the wind-driven model distribution. In particular, drifters carried around the periphery of the Canada Basin by the Beaufort gyre showed relatively few eddies to the north and east of the Alaskan Beaufort shelf and more frequent eddy encounters directly offshore of the shelf and to the west of Barrow

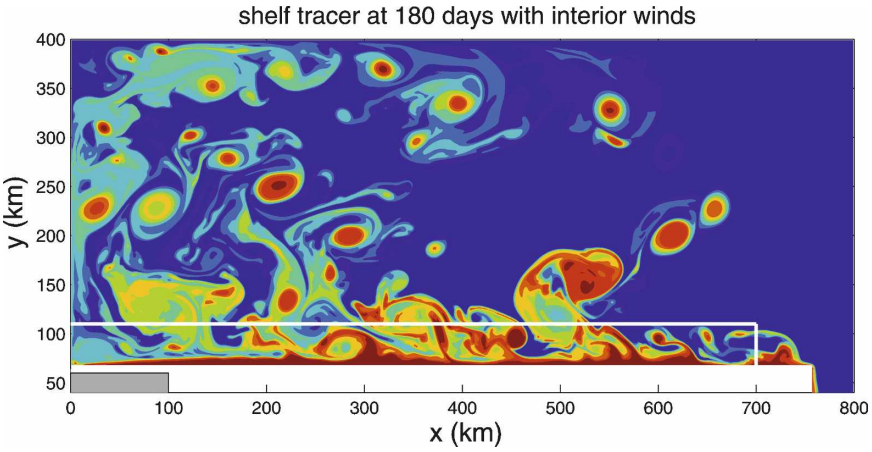

FIG. 17. Passive tracer in the model on day 180 at 115-m depth for the case with a wind-forced anticyclonic gyre in the interior.

Canyon (Krishfield and Plueddemann 2002). Although intriguing, this evidence is not definitive because the observations are only along the drift tracks and thus do not uniformly sample the region. The eddies in the wind-driven case are also smaller, on average, than the case without wind. This is most likely due to the enhanced offshore transport of the eddies by the mean flow reducing the eddy–eddy mergers that are common in the calculation without wind forcing.

The average tracer flux carried into the interior over the final 100 days is increased to 80% of the flux off the shelf, which is significantly larger than the calculation without the wind. This is due, in part, to the advection by the wind-driven flow carrying the eddies away from the boundary in the western part of the domain. There is also now an offshore transport resulting from the mean flow because the boundary current transport is diverted offshore. The wind causes an enhanced horizontal shear of the velocity field resulting from the westward flow adjacent to the boundary current; however, the energetics of this calculation look very much like that for the central calculation with no wind, so it does not appear that the instability process is strongly influenced by the wind.

c. *Parameter sensitivities*

1) LATERAL BOUNDARY CONDITION AND VISCOSITY

The structure of the lateral shear of the boundary current is fundamental to the model boundary current stability and the formation of the eddies. A model calculation identical to the standard case, except for free-slip (instead of no slip) lateral boundary conditions, produces neither eddies nor offshore flux of the passive tracer. The primary difference in the mean boundary current structure between these two calculations is the presence of a viscous shear layer near the boundary for the calculation with no-slip boundary conditions. The mean zonal velocity at 115-m depth, averaged over the final 100 days of integration and between 200- and 700-km longitude, is shown in Fig. 18 for both the free- and no-slip calculations. The velocity with free slip increases toward the boundary across the eastward-flowing boundary current to a maximum of approximately 60 cm s^{-1} with very little decay as the boundary is approached. The no-slip calculation has a much weaker maximum velocity, approximately 20 cm s^{-1}, and decreases toward zero within about 2 km of the boundary (relative vorticity $\approx -0.7f$). The offshore relative vorticity is much larger for free slip than it is for no slip, but it is positive throughout nearly the entire eastward-flowing boundary current. In contrast, the vorticity has a narrow region of large negative values for no-slip boundary conditions. The isopycnal slope is of the same sign in both cases, although significantly steeper in the free-slip case. The change in stability is likely not a result of changes in the baroclinicity of the boundary current but instead is related to the presence of the shear layer near the boundary. A similar destabilizing influence of lateral shear layers provided by no-slip boundary conditions for baroclinic instability has been found by Mundt et al. (1995) and Berloff and McWilliams (1999).

The size and growth rate of the eddies is also sensitive to the nondimensional viscosity parameter ν_s. Increased values result in larger eddies and an enhanced offshore transport of shelf tracer, while smaller values result in smaller eddies and less offshore transport (see Table 1), although in all cases studied in the range of

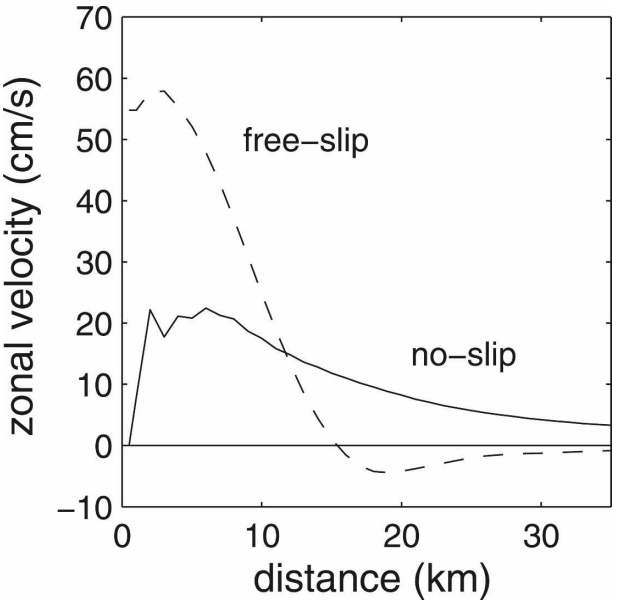

FIG. 18. Mean zonal velocity at 115-m depth for no-slip and free-slip boundary conditions.

$0.75 < \nu_s < 1.5$ the model instability appears to be qualitatively similar. The shear layer on the onshore side of the mean boundary current is the same width in all of these cases—O(2 km)—so the eddy scale is not simply related to the width of the shear layer.

2) BOTTOM SLOPE

The percent of the passive tracer that gets carried into the basin interior by eddies is sensitive to the topographic slope between the shelf break and the interior. The offshore flux increases with increasing slope, largely resulting from the production of more eddies (Table 1). The offshore flux is less than 10% for a topographic slope of 0.01 and over 90% for a bottom slope of 0.03. This suggests that the offshore flux of boundary current water might vary strongly with location as the topographic slope changes along the boundary.

TABLE 1. Normalized offshore tracer flux F for variations in Smagnorinsky viscosity coefficient ν_s; bottom slope s; and ice drag coefficient C_D.

Run	s	C_D	ν_s	F
1	0.02	2×10^{-4}	1.0	0.53
2	0.02	2×10^{-4}	0.75	0.11
3	0.02	2×10^{-4}	1.5	0.91
4	0.01	2×10^{-4}	1.0	0.07
5	0.03	2×10^{-4}	1.0	0.93
6	0.02	4×10^{-4}	1.0	0.53
7	0.02	0×10^{-4}	1.0	0.60
8	0.01	2×10^{-4}	1.5	0.73

The topographic slope at the mooring array location is approximately 0.018, close to that used for the central model calculation. However, the main point of these calculations is to demonstrate which parameters of the model are most important for the formation of eddies and the offshore flux of shelf water. The important result is that realistic topographic slopes along the Chukchi and southern Beaufort shelf break fall within the range of topographic slopes for which we find significant eddy formations and the offshore flux of tracer. However, because the offshore flux is also sensitive to the value of the viscosity coefficient ν_s, the effect of varying the bottom slope is relative; increasing the viscosity to $\nu_s = 1.5$ results in significant offshore tracer flux even when the bottom slope is relatively weak, $s = 0.01$ (Table 1).

This stabilization with decreasing bottom slope is opposite to what would be expected for a uniform baroclinic flow over a sloping bottom. However, for the boundary-trapped baroclinic boundary current here, the locations of strong potential vorticity gradients become further offset laterally as the bottom slope decreases. For example, in Fig. 9b, as the bottom slope decreases, the region of positive π_y at 100-m depth becomes offset toward the south compared to the region of negative π_y at 200-m depth. For a bottom slope less than f/N, which is about 0.01 for the present stratification, the upper part of a boundary current of width equal to the internal deformation radius will become laterally offset from the lower part of the boundary current. Spall and Pedlosky (2008) show that the growth rate of the most unstable baroclinic mode rapidly decreases as the regions of PV gradients become laterally offset, consistent with the stabilization found here.

3) ICE DRAG

The quadratic drag applied to the uppermost level in the model represents the interaction with ice cover, and damps the upper ocean motions with a time scale of O(25 days). This affects the cyclonic eddy partners that are formed during the instability process most strongly and helps to propagate the anticyclonic eddies away from the shelfbreak jet. Setting this drag to zero increases the offshore eddy flux by only 7%, while doubling it to 4×10^{-4} does not change the offshore flux at all (Table 1). Thus, the magnitude of the offshore flux is not very sensitive to variations of the drag coefficient. The drag coefficient would have to be sufficiently strong to spin down the cyclonic circulation on a time scale less than the instability time scale, which is only a

few days in these calculations, in order to significantly reduce the ability of the eddies to transport shelf tracer offshore.

5. Summary

It has been known for some time that the southern Canada Basin is populated with a large number of cold-core, anticyclonic halocline eddies. While the properties of the eddies indicate a shelf source, the mechanism of formation has been unclear. Using high-resolution mooring observations and an idealized numerical model, we have demonstrated that such eddies are likely spawned by the shelfbreak jet via baroclinic instability. Our analysis focuses on the spring time period, when winter-transformed waters from the Bering and Chukchi Seas are carried eastward by the current. These waters are near the freezing point and are very weakly stratified, forming a bottom-trapped low potential vorticity boundary current when the winds are weak. The salinity of these winter water masses ranges between 32 and 34, and are thus of interest for ventilation of both the upper and lower halocline. A mooring array 150 km east of Barrow Canyon measured an eastward transport of 0.42 Sv during periods when the boundary current is not strongly influenced by local winds. The maximum observed mean velocities were $O(25\ \mathrm{cm\ s^{-1}})$, with a current width of $O(10\text{–}15\ \mathrm{km})$. The current was highly time dependent and nonlinear, with the relative vorticity and tilting vorticity terms often becoming important for the overall Ertel potential vorticity. The eddy density and momentum fluxes calculated from the array show significant cross-stream fluxes of both density and zonal momentum. The energy conversion terms associated with these eddy fluxes indicate that the current is both baroclinically and barotropically unstable, although the baroclinic conversion term is dominant.

An idealized numerical model forced by weakly stratified dense water flowing off a shelf produces a boundary current in general agreement with the observations, both in its mean structure and time-dependent behavior. The model current is strongly unstable and produces numerous cold-core, anticyclonic middepth eddies that transport the shelf-origin water into the basin interior. The eddy fluxes and energy conversion terms in the model compare reasonably well with those from the mooring data; although the mooring data do not cover the full offshore extent of the eddy formation region, so a complete comparison is not possible. The structure of the eddies formed by the model compare well with typical velocity profiles of eddies measured in the basin interior by ADCPs from drifting ice stations. The model does show a sensitivity of the quantitative behavior (number of eddies formed and size of eddies) to details of the model configuration (bottom slope and frictional parameterizations), but the qualitative behavior is largely unchanged. The model is not intended to provide a detailed prediction of the shelfbreak jet system in the southern Beaufort Sea, but is instead used to demonstrate a plausible process and to identify parameters that are important for the stability of the shelfbreak jet. The results suggest regions in which large eddy-driven exchange can be expected (steep topography) and can isolate physical processes that need to be better understood (shear layers and mixing near topography).

The positive comparisons between the model and the data, both in the region of eddy formation and in the basin interior, suggest that the model is faithfully representing the boundary current and its instability. The number of cold-core eddies estimated to exist at any one time in the basin interior, $O(100\text{–}200)$, together with their estimated lifetime of $O(1\text{–}2\ \mathrm{yr})$, indicates that approximately 100–200 eddies are formed each year (see also Pickart et al. 2005). Based on the 2-yr mooring dataset, winter water is present along the shelf break for roughly half of the year (keep in mind that we considered only the coldest winter water in this study), which requires the formation of an eddy approximately every 1–2 days. Such a large production rate seems unlikely to be supported by only one or two canyon outflows; however, this is not unreasonable based on the number of eddies formed in the model when the entire length of the shelf break is taken into consideration. The eddies in the central model calculation flux almost half of the original shelf water into the basin interior over a boundary extent of 600 km, indicating that the eddies are quite effective at transporting water masses and properties from the shelf region into the basin interior. This suggests that eddy formation is a major contributor to halocline ventilation in the western Arctic.

The mass transport of the boundary current is much more closely confined to the boundary region than the tracer, because the eddies are not an effective means to transport momentum. However, when large-scale anticyclonic winds over the Beaufort Sea are included in the model, the slight offshore shift of the boundary current driven by the eddy fluxes is sufficient to get the boundary current transport entrained into the westward-flowing wind-driven Beaufort gyre. This results in a reduction of the eastward transport along the boundary and can result in a majority of the shelf water being transferred into the interior. One ramification of this is that an enhanced Beaufort gyre might significantly re-

direct the Pacific-origin water into the interior of the Canada Basin. Steele et al. (2004) argue that the atmosphere–ocean conditions associated with the phase of the Arctic Oscillation (AO) strongly dictate the ability for Chukchi/Bering summer water to appear north of Ellesmere Island (and subsequently flow through the Nares and Fram Straits). They attribute this to a shift in the location and strength of the transpolar drift and Beaufort gyre resulting from the AO. Our results suggest that the redirection of the boundary current may also play an important role (we note that Bering/Chukchi summer water is dense enough to flow eastward as a bottom-trapped boundary current). This is not inconsistent with Steele et al.'s scenario, but could contribute to it. Further work is required to flesh this out.

Parameterization of the tracer flux carried by these eddies in models without sufficient resolution to explicitly resolve their formation will be difficult. The eddy flux depends on details of the current structure, including the potential vorticity profile, boundary layer structure, and transport, as well as the local topography. Another difficulty in parameterizing these eddies lies in the fact that their tracer flux divergence is a nonlocal process; they are formed in one region, propagate relatively far away over a long time period, and deposit their tracers in another region through a decay process that we have not explored at all.

Acknowledgments. The authors wish to thank Anna Nikolopoulos and Daniel Torres for their help in processing and interpreting the mooring data. This study was supported by the National Science Foundation Office of Polar Programs under Grants 0421904 and 035268 (MS), and by the Office of Naval Research Grant N00014-02-1-0317 (RP and PF). Analysis by AJP was supported by the Office of Naval Research under Grant N00014-97-1-0135 and by the National Science Foundation under Grant OPP-9815303. Any opinions, findings, and conclusions or recommendations expressed in this material are those of the authors and do not necessarily reflect the views of the National Science Foundation or the Office of Naval Research.

REFERENCES

Aagaard, K., 1984: The Beaufort Undercurrent. *The Alaskan Beaufort Sea: Ecosystems and Environments,* P. W. Barnes, D. M. Schell, and E. Reimnitz, Eds., Academic Press, 47–71.

——, and E. C. Carmack, 1994: The Arctic and climate. *The Polar Oceans and Their Role in Shaping the Global Environment, Geophys. Monogr.,* No. 85, Amer. Geophys. Union, 4–20.

——, L. K. Coachman, and E. C. Carmack, 1981: On the halocline of the Arctic Ocean. *Deep-Sea Res.,* **28,** 529–545.

Berloff, P. S., and J. C. McWilliams, 1999: Quasigeostrophic dynamics of the western boundary current. *J. Phys. Oceanogr.,* **29,** 2607–2634.

Bush, A. B. G., J. C. McWilliams, and W. R. Peltier, 1996: The formation of oceanic eddies in symmetric and asymmetric jets. Part II: Late time evolution and coherent vortex formation. *J. Phys. Oceanogr.,* **26,** 1825–1848.

Chao, S.-Y., and P.-T. Shaw, 1996: Initialization, asymmetry, and spindown of Arctic eddies. *J. Phys. Oceanogr.,* **26,** 2076–2092.

——, and ——, 1998: Eddy maintenance and attrition in a vertically sheared current under Arctic ice. *J. Phys. Oceanogr.,* **28,** 2427–2443.

——, and ——, 2002: A numerical investigation of slanted convection and subsurface anticyclone generation in an Arctic baroclinic current system. *J. Geophys. Res.,* **107,** 3019, doi:10.1029/2001JC000786.

——, and ——, 2003a: A numerical study of dense water outflows and halocline anticyclones in an Arctic baroclinic slope current. *J. Geophys. Res.,* **108,** 3226, doi:10.1029/2002JC001473.

——, and ——, 2003b: Heton shedding from submarine-canyon plumes in an Arctic boundary current system: Sensitivity to the undercurrent. *J. Phys. Oceanogr.,* **33,** 2032–2044.

Coachman, L. K., K. Aagaard, and R. B. Tripp, 1975: *Bering Strait: The Regional Physical Oceanography*. University of Washington Press, 172 pp.

D'Asaro, E. A., 1988a: Observations of small eddies in the Beaufort Sea. *J. Geophys. Res.,* **93,** 6669–6684.

——, 1988b: Generation of submesoscale vortices: A new mechanism. *J. Geophys. Res.,* **93,** 6685–6693.

Fratantoni, P. S., S. Zimmerman, R. S. Pickart, and M. Swartz, 2006: Western Arctic Shelf-Basin Interactions Experiment: Processing and calibration of moored profiler data from the Beaufort shelf edge mooring array. Woods Hole Oceanographic Institution Tech. Rep. WHOI-2006-15, 34 pp.

Hall, M. M., 1994: Synthesizing the Gulf Stream thermal structure from XBT data. *J. Phys. Oceanogr.,* **24,** 2278–2287.

Hart, J. E., and P. D. Killworth, 1976: Open ocean baroclinic instability in the Arctic. *Deep-Sea Res.,* **23,** 637–645.

Hogg, N. G., and H. M. Stommel, 1985: The heton, an elementary interaction between discrete baroclinic geostrophic vortices and its implications concerning eddy heat-flow. *Proc. Roy. Soc. London,* **A397,** 1–20.

Hunkins, K. L., 1974: Subsurface eddies in the Arctic Ocean. *Deep-Sea Res.,* **21,** 1017–1033.

Krishfield, R. A., and A. J. Pluddemann, 2002: Eddies in the Arctic Ocean from IOEB ADCP data. Woods Hole Oceanographic Institution Tech. Rep. WHOI-2002-09, 144 pp.

Kulikov, E. A., E. C. Carmack, and R. W. Macdonald, 1998: Flow variability at the continental shelf break of the Mackenzie Shelf in the Beaufort Sea. *J. Geophys. Res.,* **103,** 12 725–12 741.

Llinas, L., R. S. Pickart, J. T. Mathis, and S. L. Smith, 2008: The effects of eddy transport on zooplankton biomass and community composition in the western Arctic. *Deep-Sea Res. II,* in press.

Manley, T. O., and K. Hunkins, 1985: Mesoscale eddies of the Arctic Ocean. *J. Geophys. Res.,* **90,** 4911–4930.

Marshall, J., C. Hill, L. Perelman, and A. Adcroft, 1997: Hydrostatic, quasi-hydrostatic, and non-hydrostatic ocean modeling. *J. Geophys. Res.,* **102,** 5733–5752.

Mathis, J. T., R. S. Pickart, D. A. Hansell, D. Kadko, and N. R. Bates, 2007: Eddy transport of organic carbon and nutrients from the Chukchi Shelf into the deep Arctic basin. *J. Geophys. Res.,* **112,** C05011, doi:10.1029/2006JC003899.

Melling, H., 1998: Hydrographic changes in the Canada basin of the Arctic ocean, 1979–1996. *J. Geophys. Res.,* **103,** 7637–7645.

Mountain, D. G., L. K. Coachman, and K. Aagaard, 1976: On the flow through Barrow Canyon. *J. Phys. Oceanogr.,* **6,** 461–470.

Muench, R. D., J. D. Schumacher, and S. A. Salo, 1988: Winter currents and hydrographic conditions on the northern central Bering Sea shelf. *J. Geophys. Res.,* **93,** 516–526.

——, J. T. Gunn, T. E. Whitledge, P. Schlosser, and W. Smethie Jr., 2000: An Arctic Ocean cold core eddy. *J. Geophys. Res.,* **105,** 23 997–24 006.

Münchow, A., and E. Carmack, 1997: Synoptic flow and density observations near an Arctic shelfbreak. *J. Phys. Oceanogr.,* **27,** 1402–1419.

——, R. S. Pickart, T. J. Weingartner, R. A. Woodgate, and D. Kadko, 2006: Arctic boundary currents over the Chukchi and Beaufort slope seas: Observational snapshots, transports, scales, and spatial variability from ADCP surveys. *Eos, Trans. Amer. Geophys. Union,* **87** (Ocean Science Meeting Suppl.), Abstract OS33N-03.

Mundt, M. D., N. H. Brummell, and J. E. Hart, 1995: Linear and nonlinear baroclinic instability with rigid sidewalls. *J. Fluid Mech.,* **291,** 109–138.

Newton, J. L., K. Aagaard, and L. K. Coachman, 1974: Baroclinic eddies in the Arctic Ocean. *Deep-Sea Res.,* **21,** 707–719.

Nikolopoulos, A., R. S. Pickart, P. S. Fratantoni, K. Shimada, D. J. Torres, and E. P. Jones, 2008: The western Arctic boundary current at 152W: Structure, variability, and transport. *Deep-Sea Res. II,* in press.

Ou, H. W., and A. L. Gordon, 1986: Spin-down of baroclinic eddies under sea ice. *J. Geophys. Res.,* **91,** 7623–7630.

Paquette, R. G., and R. H. Bourke, 1974: Observations on the coastal current of Arctic Alaska. *J. Mar. Res.,* **32,** 195–207.

Pedlosky, J., 1985: The instability of continuous heton clouds. *J. Atmos. Sci.,* **42,** 1477–1486.

Pickart, R. S., 2004: Shelfbreak circulation in the Alaskan Beaufort Sea: Mean structure and variability. *J. Geophys. Res.,* **109,** C04024, doi:10.1029/2003JC001912.

——, T. J. Weingartner, L. J. Pratt, S. Zimmermann, and D. J. Torres, 2005: Flow of winter-transformed Pacific water into the Western Arctic. *Deep-Sea Res. II,* **52,** 3175–3198.

Plueddemann, A. J., R. Krishfield, T. Takizawa, K. Hatakeyama, and S. Honjo, 1998: Upper ocean velocities in the Beaufort Gyre. *Geophys. Res. Lett.,* **25,** 183–186.

Roach, A. T., A. Aagaard, C. H. Pease, S. A. Salo, T. Weingartner, V. Pavlov, and M. Kulakov, 1995: Direct measurements of transport and water properties through Bering Strait. *J. Geophys. Res.,* **100,** 18 443–18 457.

Shimada, K., and A. Kubokawa, 1997: Nonlinear evolution of linearly unstable barotropic boundary currents. *J. Phys. Oceanogr.,* **27,** 1326–1348.

——, E. C. Carmack, K. Hatakeyama, and T. Takizawa, 2001: Varieties of shallow temperature maximum waters in the Western Canadian Basin of the Arctic Ocean. *Geophys. Res. Lett.,* **28,** 3441–3444.

Smagorinsky, J., 1963: General circulation experiments with the primitive equations: I. The basic experiment. *Mon. Wea. Rev.,* **91,** 99–164.

Spall, M. A., 1995: Frontogenesis, subduction, and cross-front exchange at upper ocean fronts. *J. Geophys. Res.,* **100,** 2543–2557.

——, and J. Pedlosky, 2008: Lateral coupling in baroclinically unstable flows. *J. Phys. Oceanogr.,* **38,** 1267–1277.

Steele, M., R. Morley, and W. Ermold, 2001: PHC: A global ocean hydrography with a high-quality Arctic Ocean. *J. Climate,* **14,** 2079–2087.

——, J. Morrison, W. Ermold, I. Rigor, and M. Ortmeyer, 2004: Circulation of summer Pacific halocline water in the Arctic Ocean. *J. Geophys. Res.,* **109,** C02027, doi:10.1029/2003JC002009.

Sutyrin, G. G., 1992: Maintenance of quick fluid rotation in the cores of long-lived oceanic eddies. *J. Mar. Syst.,* **3,** 489–496.

Timmerman, M.-L., J. Toole, A. Proshutinsky, R. Krishfield, and A. Plueddemann, 2008: Eddies in the Canada Basin, Arctic Ocean, observed from ice-tethered profilers. *J. Phys. Oceanogr.,* **38,** 133–145.

Weingartner, T. J., D. J. Cavalieri, K. Aagaard, and Y. Sasaki, 1998: Circulation, dense water formation, and outflow on the northeast Chukchi shelf. *J. Geophys. Res.,* **103,** 7647–7661.

CORRIGENDUM

MICHAEL A. SPALL, ROBERT S. PICKART, PAULA S. FRATANTONI, AND ALBERT J. PLUEDDEMANN

Woods Hole Oceanographic Institution, Woods Hole, Massachusetts

Due to production errors, Figs. 5, 6, 7, and 15 of Spall et al. (2008) were presented incorrectly. Panel titles and color bar labels were cut off. The correct figures as they were meant to appear are shown below.

The staff of the *Journal of Physical Oceanography* regrets any inconvenience these errors may have caused.

REFERENCE

Spall, M. A., R. S. Pickart, P. S. Fratantoni, and A. J. Plueddemann, 2008: Western Arctic shelfbreak eddies: Formation and transport. *J. Phys. Oceanogr.,* **38,** 1644–1668.

E-mail: mspall@whoi.edu

DOI: 10.1175/2010JPO4483.1

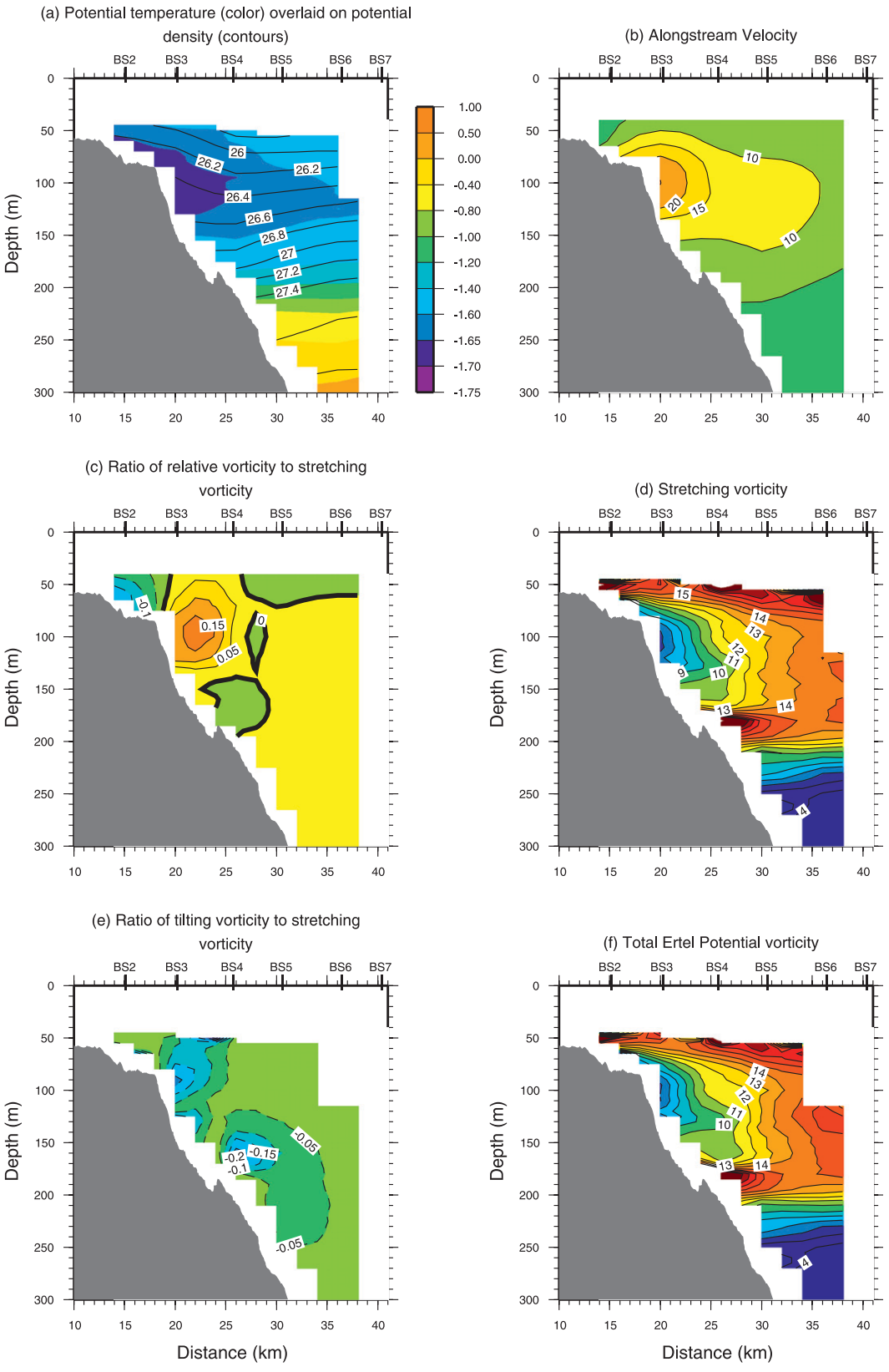

FIG. 5. (a)–(f) Mean vertical sections of the unforced jet.

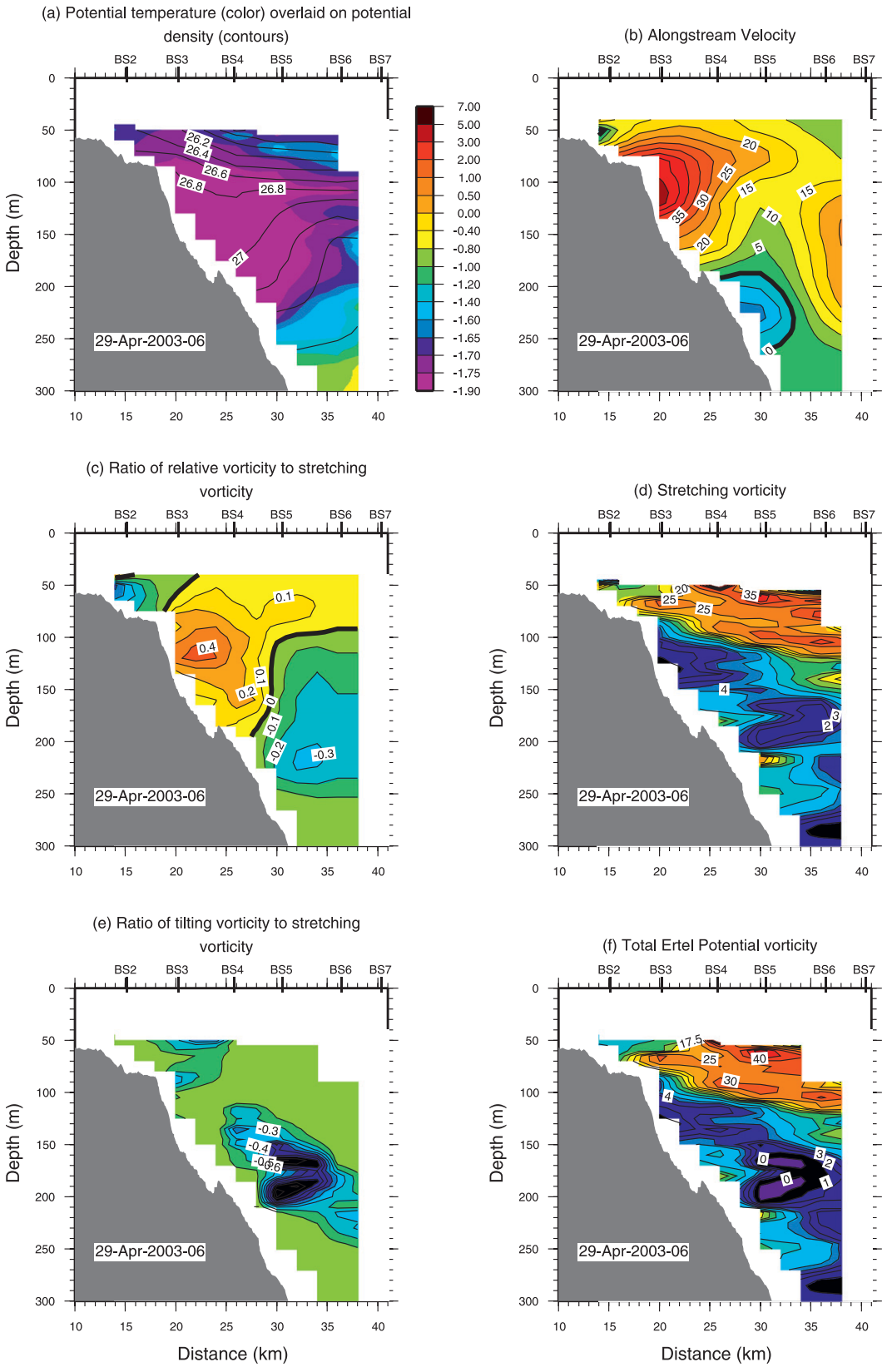

FIG. 6. (a)–(f) Vertical sections of a snapshot of the jet at 0600 UTC 29 Apr 2003.

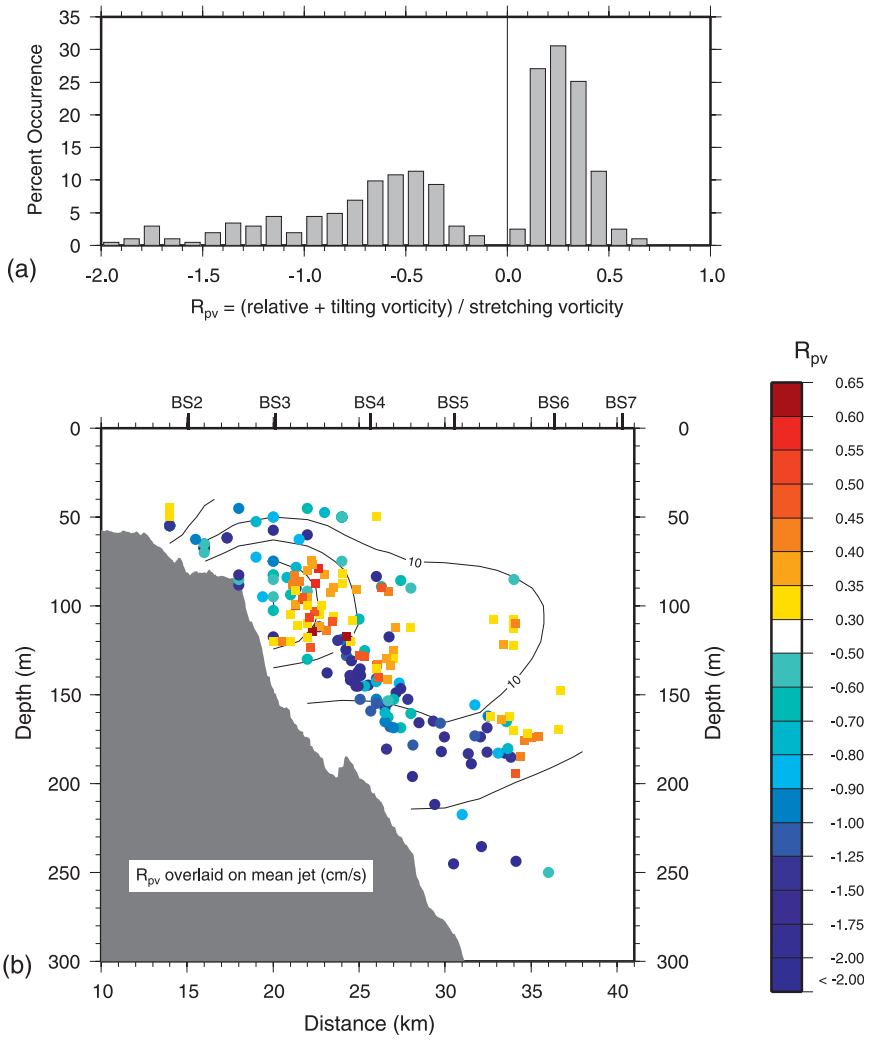

FIG. 7. (a) Histogram of the positive and negative extrema of R_{pv} for the collection of sections. (b) Scatterplot of the extrema of R_{pv} overlaid on the mean along-stream velocity section of Fig. 5.

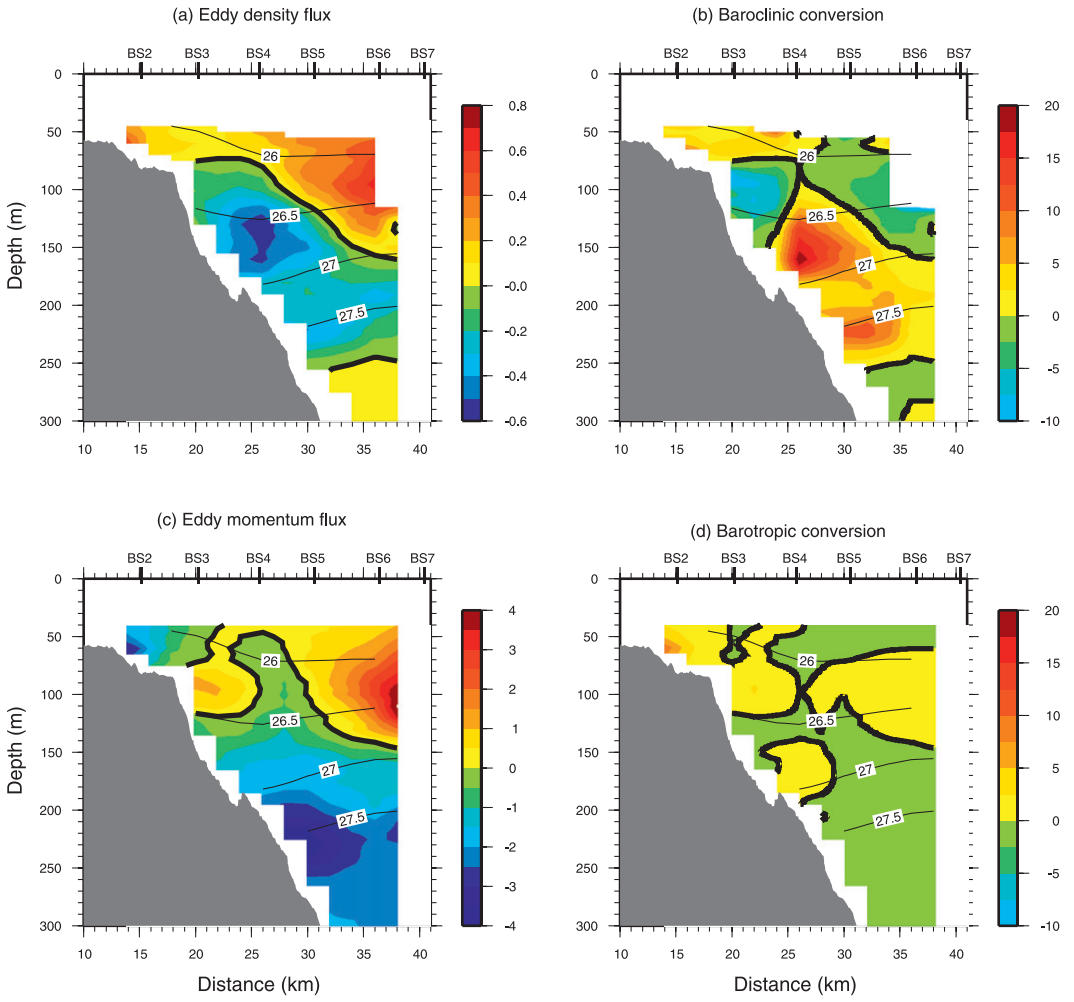

FIG. 15. Results from the mooring data for the (a) offshore eddy density flux (kg m^{-2} s^{-1} $\times$ 10^{-2}), (b) baroclinic energy conversion term [(6); m^2 s^{-3} $\times$ 10^{-8}), (c) eddy momentum flux (m^2 s^{-2} $\times$ 10^{-3}), and (d) barotropic energy conversion term [(7); m^2 s^{-3} $\times$ 10^{-8}].